Evaluation of Longitudinal Double-Spin Asymmetry Measurements in Semi-Inclusive Deep-Inelastic Scattering from the Proton for the ECCE Design

May 16, 2022

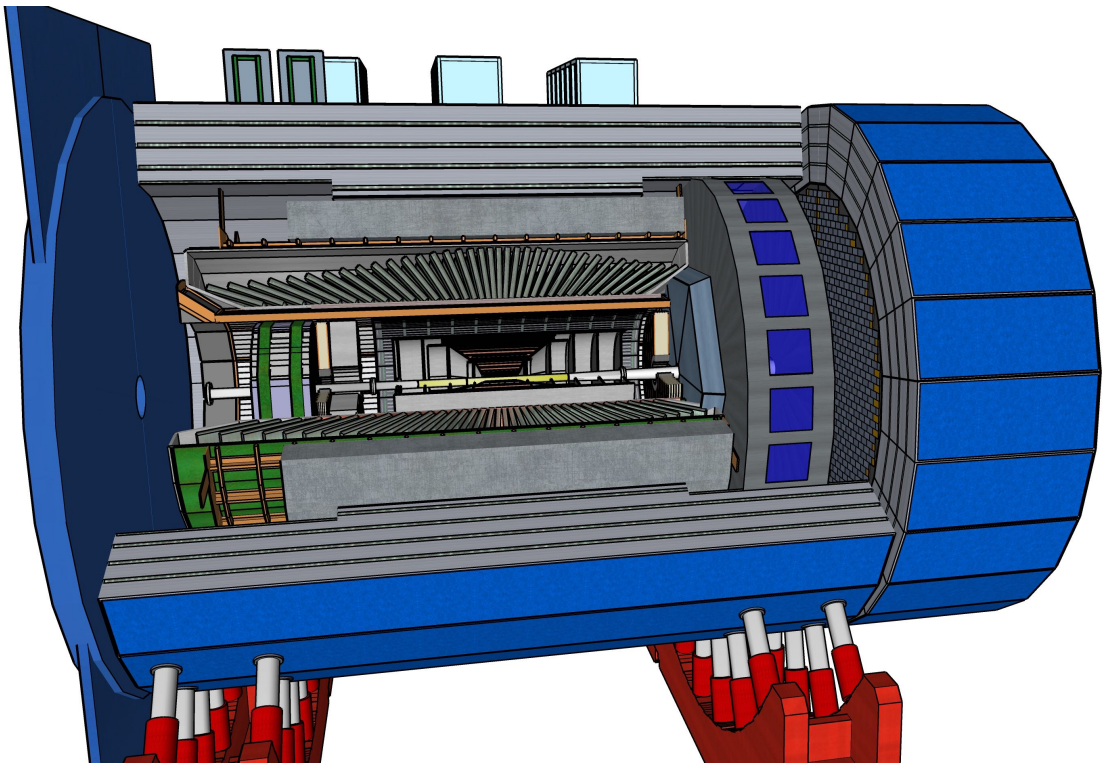

ecce-note-[phys]-2022-03
v0.1

ecce-note-[phys]-2022-03
v0.1
May 16, 2022

Evaluation of Longitudinal Double-Spin Asymmetry Measurements in Semi-Inclusive Deep-Inelastic Scattering from the Proton for the ECCE Design

ECCE consortium*

Abstract

The evaluation of the measurement of double-spin asymmetries for charge-separated pions and kaons produced in deep-inelastic scattering from the proton using the ECCE detector design concept is presented, for the combinations of lepton and hadron beam energies of 5×41 GeV^2 and 18×275 GeV^2. The study uses unpolarised simulated data that is processed through a full GEANT simulation of the detector. These data are then reweighted at the parton level with DSSV helicity distributions and DSS fragmentation functions, in order to generate the relevant asymmetries, and subsequently analysed. The performed analysis shows that the ECCE detector concept provides the resolution and acceptance, with a broad coverage in kinematic phase space, needed for a robust extraction of asymmetries. This, in turn, allows for a precise extraction of sea-quark helicity distributions.

*Authors are listed at the end of this paper

Contents

1 Introduction

The measurement of the longitudinal double-spin asymmetry in deep-inelastic scattering (DIS) provides an experimentally clean access to the parton helicity distributions. The asymmetry is proportional to the sum of convolutions of parton helicity distributions and fragmentation functions, where the convolutions are weighted by the charge squared of the parton struck in the DIS process. Through the measurement of asymmetries in semi-inclusive DIS, where the formed hadron is tagged, one gains sensitivity to the parton flavour. The combined analysis of longitudinal double-spin asymmetries in inclusive and semi-inclusive DIS as well as in proton-proton collisions already provide constraints on parton helicity distributions at moderate Bjorken-x, x_B [1]. Yet, because of absence of data, the sea-quark and gluon helicity distributions at lower values of x_B suffer from large uncertainties. The measurement of inclusive DIS at the EIC is expected to provide strong constraints on the gluon helicity distribution at low x_B, since the large Q^2 coverage of the EIC allows to probe Q^2 evolution, while the strength of semi-inclusive measurements at an EIC lies in the separation of the sea-quark helicity distributions. The expected performance of the ECCE-EIC detector for the measurement of longitudinal double-spin asymmetries in the production of charge-separated pions and kaons in semi-inclusive DIS is evaluated through the study of a Monte-Carlo simulation. The result of this study is presented in this note.

In section 2, the used Monte-Carlo simulations are described as well as the data selection. In section 3, the asymmetries extracted from the Monte-Carlo simulation are presented, while in section 4 the impact of the foreseen measurements on the helicity distributions are shown. Finally, in section 5, the conclusions are summarised.

2 Data selection and Monte-Carlo reweighting

The semi-inclusive DIS events were generated with the PYTHIA-6 [2] (eRHIC) Monte-Carlo simulation, using the same steering-card settings as those used for the Yellow Report [3][2]. Only the default PYTHIA initial-state and final-state radiation are included in this simulation, while dedicated radiative effects are absent. Radiative effects present in measurements can be evaluated through unfolding techniques using dedicated Monte-Carlo simulations. The generated output is passed through a full GEANT simulation of the ECCE detector. The detector configuration of the second simulation campaign, i.e., the 'July concept' [4, 5], is used to produce and reconstruct the simulated data for the here presented studies. Unless stated otherwise, the field strength of the ECCE solenoid superconducting magnet was set to 1.4 T.

Since the PYTHIA-6 Monte Carlo does not include helicity distributions, the simulated

[2]The generated data as well as the steering files are available under /gpfs02/eic/DATA/YR_SIDIS/ at RCF as well as shared via the BNL Box service.

data needs to be reweighted[3]. The applied weights are evaluated at next-to-leading order in perturbative QCD, at the generated values of the kinematic variables x_B, $Q^2 = -q^2$, and $z = (p \cdot P_h)/(p \cdot q)$, where q, p, and P_h represent the four momenta of, respectively, the virtual photon, beam proton and created hadron. The weights are of the form

$$1 + \Lambda D(y) \frac{\Delta \otimes D^{q,g \to h}}{F^h_{UU}}, \tag{1}$$

where $\Lambda = +1$ or $\Lambda = -1$ depending if the beam lepton and beam proton have their spin orientation respectively parallel or anti-parallel. The respective orientation of the spin of the lepton and proton beams is for each event randomly simulated. The depolarisation factor is represented by $D(y)$, where y is the inelasticity. The depolarisation factor depends on the ratio of the longitudinal to transverse virtual-photon absorption cross sections. For the evaluation of this ratio, the parametrisation from Ref. [6] is used. The term Δ stands for $e_q^2 \Delta q$, with e_q^2 the parton charge squared, or Δg depending if the primary parton is a quark or a gluon. The symbol $\otimes$ represents the convolution integral of the parton helicity distribution and the fragmentation function $D^{q,g \to h}$, evaluated at next-to-leading order. As input, the DSSV14 helicity distributions [1, 7] and the DSS14 pion and kaon fragmentation functions [8, 9] are used. The unpolarised structure function F_{UU} is the charge-squared weighted sum of the convolution integrals of the spin-independent PDFs and fragmentation functions. For the PDFs, the NNPDF30_nlo_as_0118 set [10], evaluated through the LHAPDF interpolator [11], is used. The next-to-leading order semi-inclusive DIS coefficients needed in the calculation are taken from Ref. [12].

	$Q^2 > 1$ GeV^2	1 GeV^2 $< Q^2 <$ 100 GeV^2	$Q^2 > 100$ GeV^2
18×275 GeV^2	21.923 pb^{-1}	21.995 pb^{-1}	1231.564 pb^{-1}
5×41 GeV^2	61.402 pb^{-1}	61.483 pb^{-1}	5944.374 pb^{-1}

Table 1: Luminosity of the various Monte-Carlo data sets, generated at the energy configurations 18×275 GeV^2 and 5×41 GeV^2.

Data have been simulated for various sets of lepton and proton beam energies: 5 GeV and 41 GeV, 10 GeV and 100 GeV, 18 GeV and 100 GeV, and 18 GeV and 275 GeV. In order to illustrate the impact of the EIC-ECCE design on the determination of the helicity distributions, the studies for data simulated at the highest and lowest centre-of-mass energies, $\sqrt{s}$, are presented. For these energies, the simulated data sets, generated for different regions in Q^2, and their corresponding luminosity are summarised in table 1. In the present study, the statistical uncertainties of the asymmetries are scaled to an integrated luminosity of 10 fb^{-1}.

For the evaluation of the double-spin asymmetries, events satisfying the following criteria are selected: $Q^2 > 1$ GeV^2, in order to be in the DIS regime, a squared invariant mass of the photon-nucleon system $W^2 > 10$ GeV^2, in order to avoid the region dominated by

[3]Only the processes with PYTHIA ID 99, 131–136 are reweighted.

x_B	1.0e-05	1.58489e-05	2.51189e-05	3.98107e-05	6.30957e-05
	1.0e-04	1.58489e-04	2.51189e-04	3.98107e-04	6.30957e-04
	1.0e-03	1.58489e-03	2.51189e-03	3.98107e-03	6.30957e-03
	1.0e-02	1.58489e-02	2.51189e-02	3.98107e-02	6.30957e-02
	1.0e-01	1.58489e-01	2.51189e-01	3.98107e-01	6.30957e-01
	1.0				
Q^2 [GeV^2]	1.0	1.77828	3.16228	5.62341	
	10.0	17.7828	31.6228	56.2341	
	100.0	177.828	316.228	562.341	
	1000.0	10000.0			
z	0.01	0.05	0.10	0.15	0.20
	0.25	0.30	0.40	0.50	0.60
	0.70	0.80	0.90	1.00	

Table 2: Used kinematic bins in x_B, Q^2, and z.

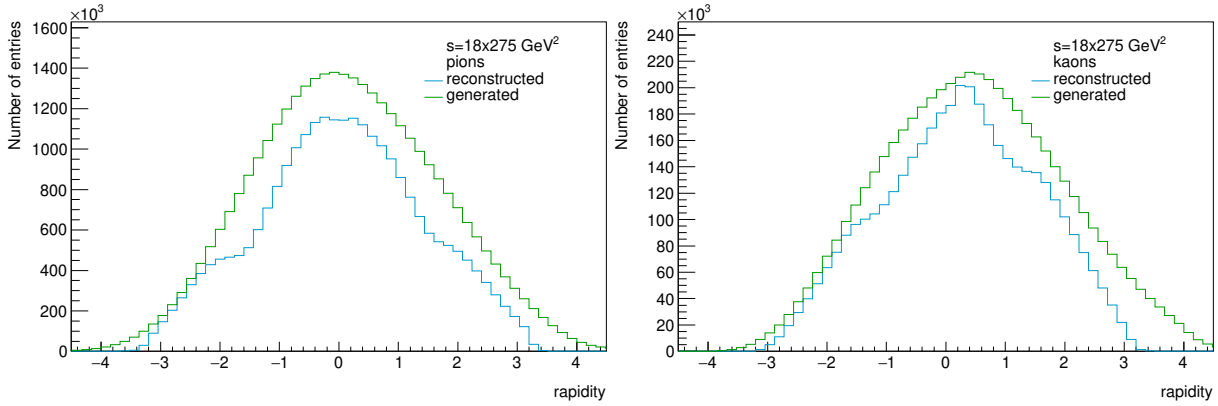

Figure 1: Rapidity distribution (in the laboratory frame) of generated (green line) and reconstructed (blue line) pions (left) and kaons (right).

baryon-resonance production, and an inelasticity $0.01 < y < 0.95$, where the upper cut aims at limiting contributions from QED radiation and the lower cut removes events with a degraded resolution in the particle's momentum reconstruction. The (reconstructed) hadrons are identified using the generated Monte-Carlo information and their fractional energy z is restricted to lie above 0.01, in order to limit contributions from target fragmentation. No special requirement is placed on the hadron rapidity. The rapidity distribution (in the laboratory frame) of the generated and reconstructed pions and kaons is presented in figure 1. The selected data sample is evaluated in 25 bins of x_B, 13 bins of Q^2, and 13 bins of z, as presented in table 2.

3 Evaluation of the asymmetries

Experimentally, clean access in semi-inclusive DIS to the helicity distributions is provided by the extraction of double-spin asymmetries. Assuming constant lepton-beam and proton-beam polarisation, respectively P_e and P_p, they can be written as:

$$\begin{aligned} A_{\parallel}^{h}(x_B, Q^2, z) &= \frac{1}{P_e P_p} \frac{\frac{\overrightarrow{N^h}}{\overrightarrow{L}} - \frac{\overleftarrow{N^h}}{\overleftarrow{L}}}{\frac{\overrightarrow{N^h}}{\overrightarrow{L}} + \frac{\overleftarrow{N^h}}{\overleftarrow{L}}}(x_B, Q^2, z) \\ &= D(y) A_1^h(x_B, Q^2, z), \end{aligned} \tag{2}$$

where $\overrightarrow{N^h}$ ($\overleftarrow{N^h}$) represents the number of semi-inclusive DIS hadrons of type h in bin (x_B, Q^2, z) collected with (anti-)parallel beam-spin orientation, while $\overrightarrow{L}$ ($\overleftarrow{L}$) is the corresponding luminosity. The asymmetry $A_{\parallel}^h$ represents the asymmetry with respect to the lepton-beam direction, while A_1^h is the asymmetry with respect to the virtual photon and gives access to the convolution of the parton helicity distributions and fragmentation functions.

In the present simulation, N^h is obtained by reweighting each event, as described in section 2, while the randomly generated relative beam-spin orientation results in $\overrightarrow{L} \approx \overleftarrow{L}$. The lepton and proton beam polarisations are set to 100% in the simulation, but in order to account for experimentally realistic conditions, a beam polarisation for both beams of 70% is assumed in the evaluation of the statistical uncertainty.

In the following, the depolarisation factor is set to 1 for the evaluation of the systematic uncertainties, both in equation 1 for the reweighting of the simulation and for the extraction of A_1 in equation 3. The reason for this approach lies in the enhancement of small differences between generated and reconstructed data points when introducing the depolarisation factor due to fluctuations that result solely from the limited amount of generated Monte-Carlo data. For the evaluation of the statistical uncertainty, the actual value of the depolarisation factor is used in equations 1 and 3 and in addition it is required to lie above 0.1.

The generated asymmetries, evaluated from the generated scattered beam-lepton and hadron information, as well as the reconstructed asymmetries, evaluated from the scattered beam lepton and created particles reconstructed by the ECCE detector, are presented in figures 2 and 3 for positive pions and in figures 4 and 5 for negative kaons, for $s = 5 \times 41$ GeV^2 and $s = 18 \times 275$ GeV^2. Corresponding figures for negative pions and positive kaons can be found in appendix A. The depolarisation factor is here set equal to 1. The different behaviour of the kaon and pion asymmetries at larger z values reflects the fact that, contrary to the pion, the negative kaon and the proton do not have a valence

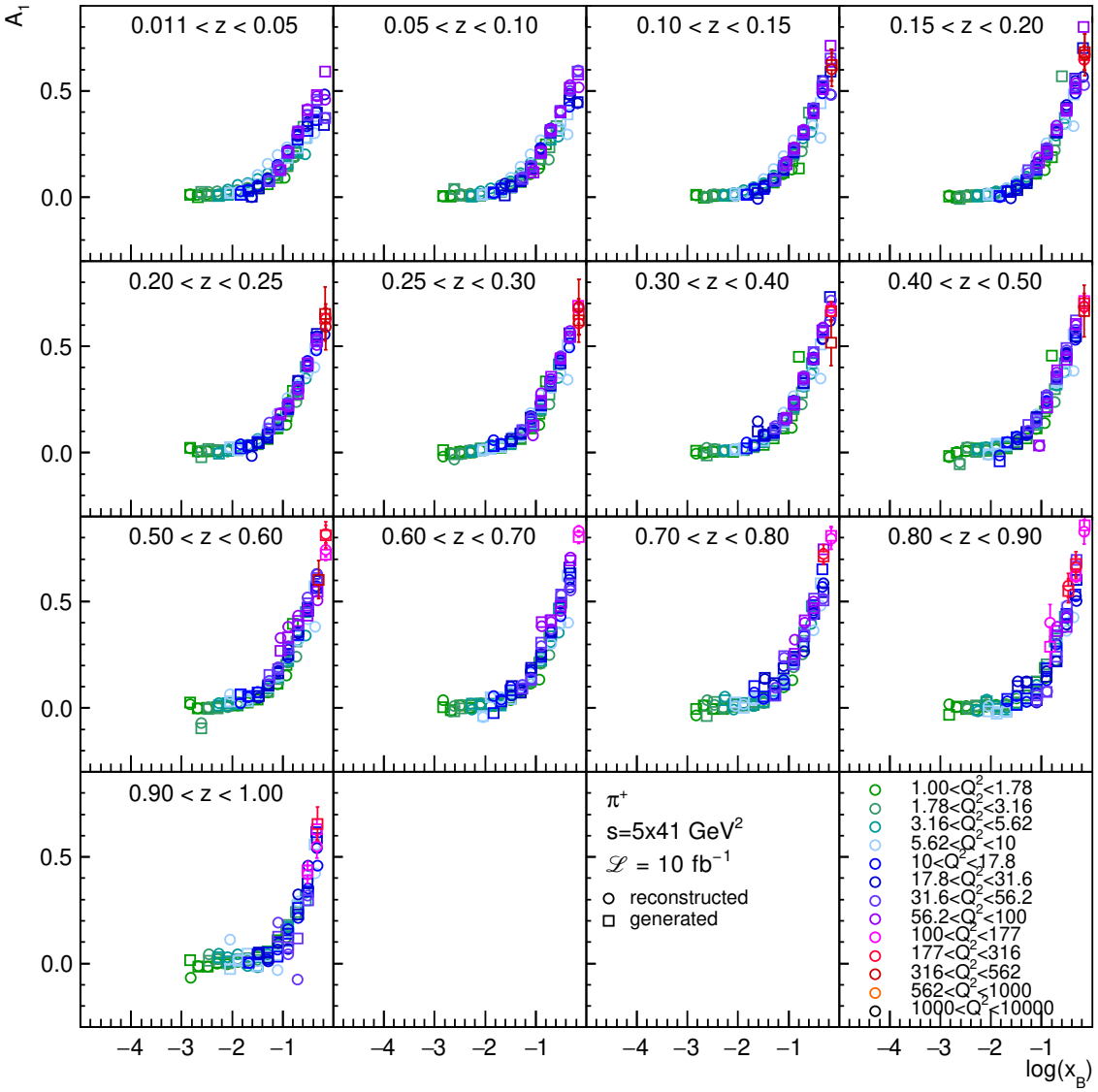

Figure 2: Generated (squares) and reconstructed (circles) double-spin asymmetries with $D(y) = 1$ for positive pions, as a function of x_B and for different ranges in z (panels) and Q^2 (colors). The data points are drawn at, respectively, the average generated and average reconstructed x_B in each bin. The data are generated at $s = 5 \times 41$ GeV^2 and scaled to an integrated luminosity of 10 fb^{-1}.

quark flavour in common. As can be seen from the figures, the reconstructed asymmetries agree quite well with the generated asymmetries, and any effect from unreconstructed hadrons or smearing of the kinematic variables due to finite detector resolution stays very limited. In that sense, the ECCE design is robust and satisfies the requirements needed for the extraction of double-spin asymmetries.

The figures also clearly show the broad kinematic coverage in x_B, Q^2, and z, with the two centre-of-mass energies covering complementary regions in x_B for the different ranges in z.

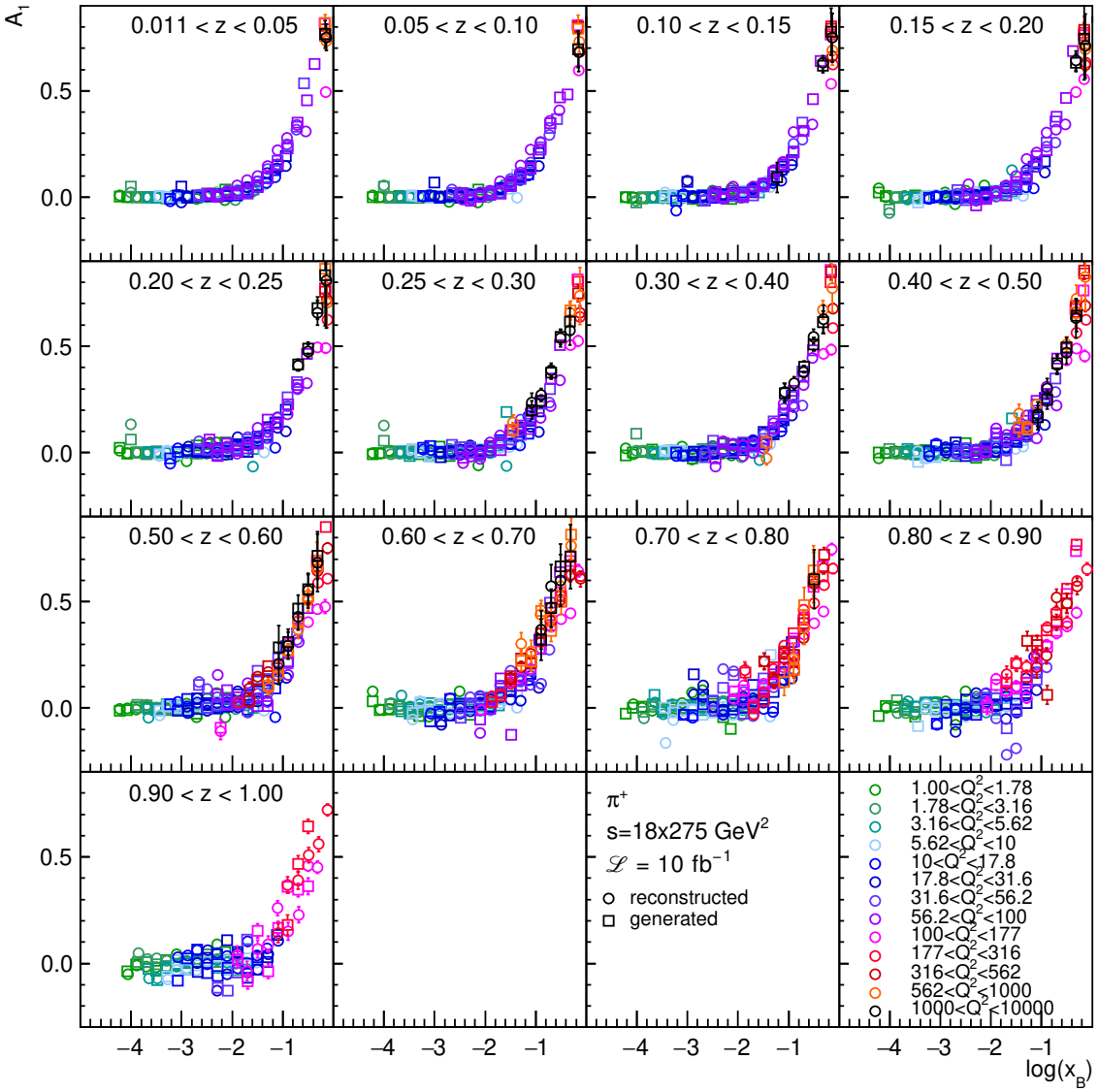

Figure 3: Generated (squares) and reconstructed (circles) double-spin asymmetries with $D(y) = 1$ for positive pions, as a function of x_B and for different ranges in z (panels) and Q^2 (colors). The data points are drawn at, respectively, the average generated and average reconstructed x_B in each bin. The data are generated at $s = 18 \times 275$ GeV^2 and scaled to an integrated luminosity of 10 fb^{-1}.

The data collected at high centre-of-mass energy allows to reach x_B values down to 10^{-4}. Such broad kinematic coverage is needed for a precise extraction of the various parton helicity distributions.

In a realistic experimental situation, an unfolding procedure would be applied to the measured asymmetry in order to extract the 'physics' asymmetry, free from detector effects. The application of such unfolding procedure in the present study would allow to extract a 'physics' asymmetry, which approaches the generated asymmetry more closely.

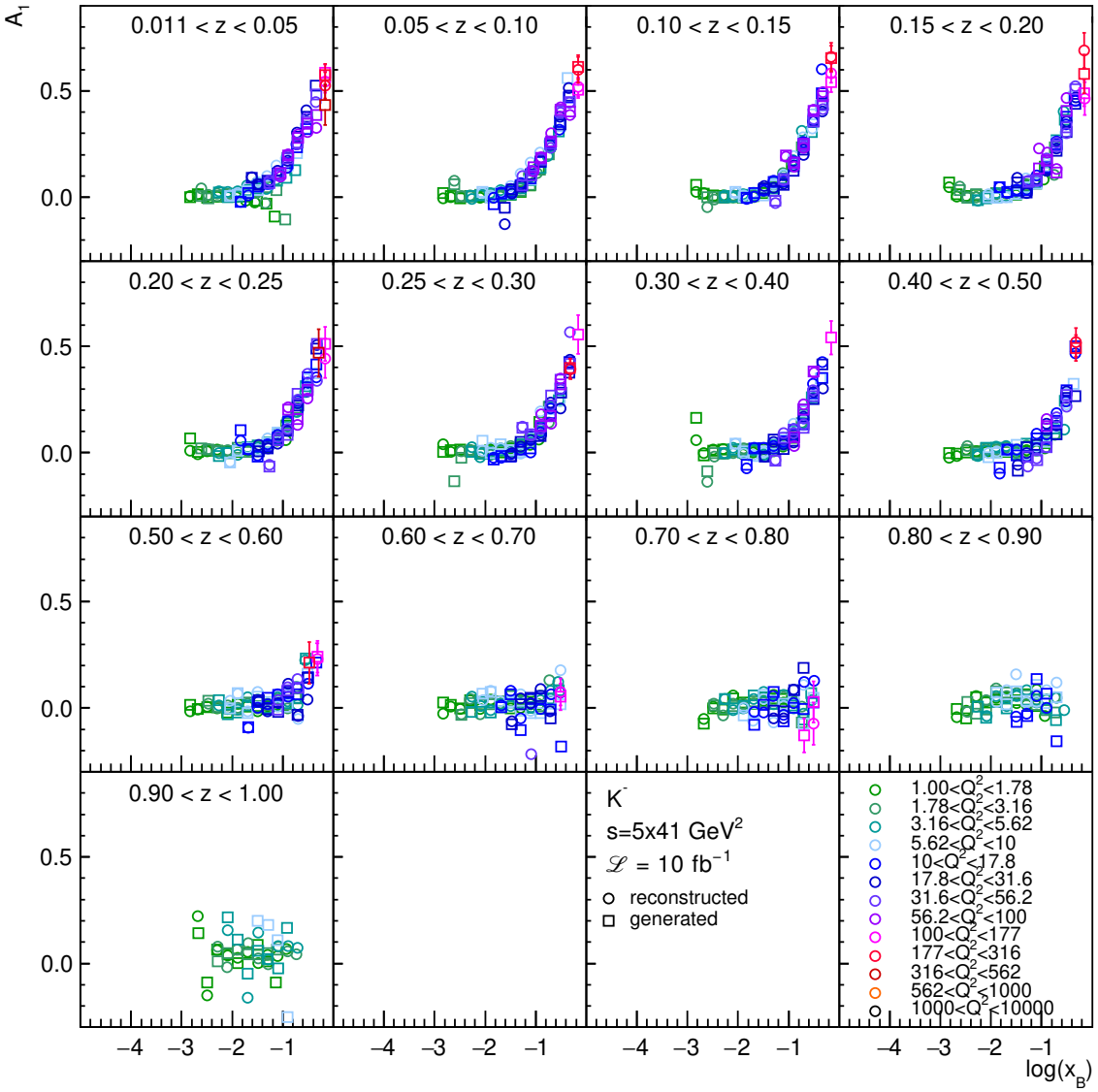

Figure 4: Generated (squares) and reconstructed (circles) double-spin asymmetries with $D(y) = 1$ for negative kaons, as a function of x_B and for different ranges in z (panels) and Q^2 (colors). The data points are drawn at, respectively, the average generated and average reconstructed x_B in each bin. The data are generated at $s = 5 \times 41$ GeV^2 and scaled to an integrated luminosity of 10 fb^{-1}.

Such unfolding would require a vastly larger sample of simulated data and an elaborate procedure, which surpasses the purpose of the present study. Instead, it is decided to take the difference between the generated and the reconstructed asymmetry as a systematic uncertainty in each kinematic (x_B, Q^2, z) bin. The corresponding evaluated uncertainty is expected to constitute an upper limit on the systematic uncertainty. In addition to this systematic uncertainty, a global scale uncertainty of 2%, stemming from the uncertainty in each of the two beam polarisations, is taken into account.

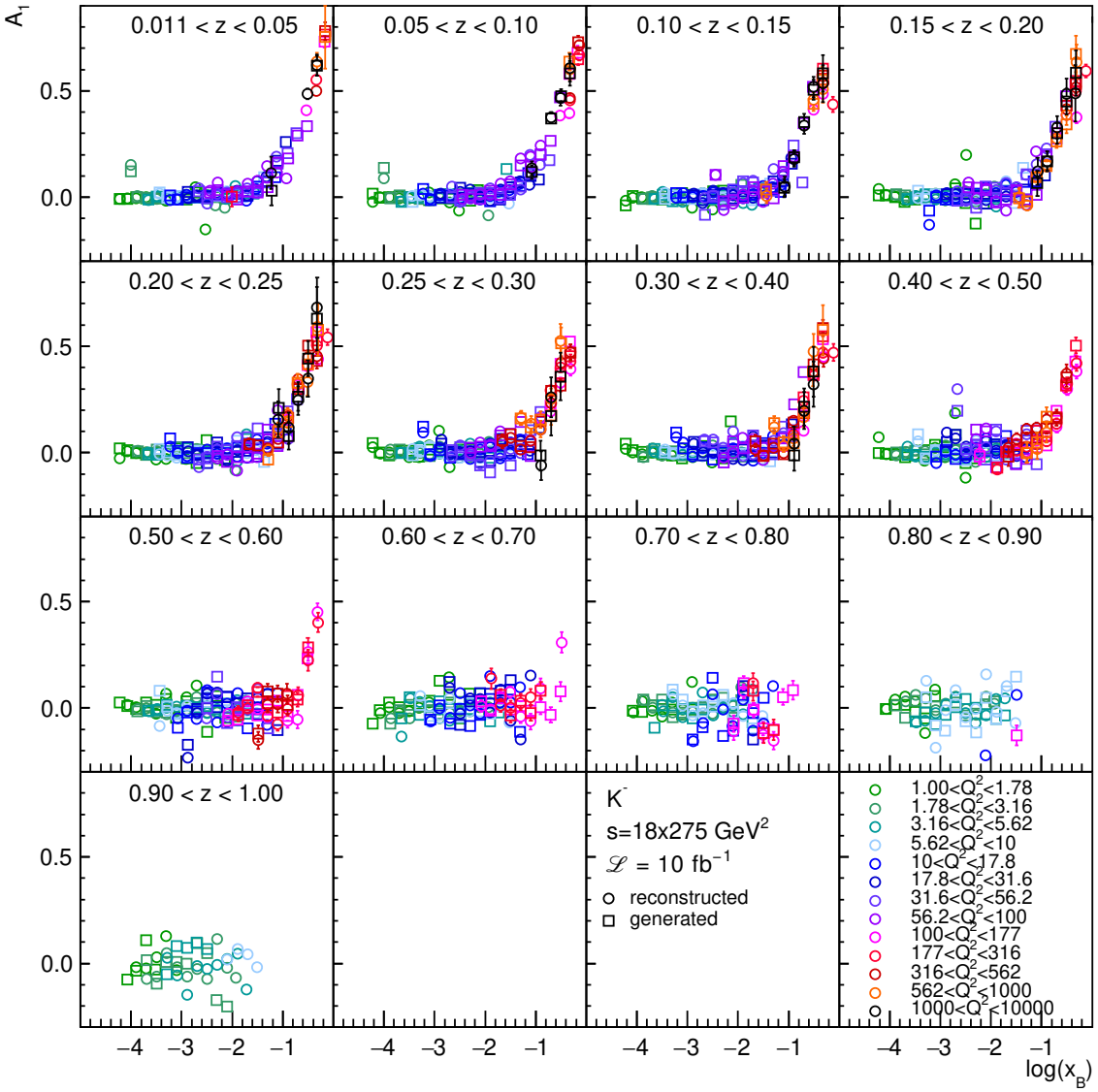

Figure 5: Generated (squares) and reconstructed (circles) double-spin asymmetries with $D(y) = 1$ for negative kaons, as a function of x_B and for different ranges in z (panels) and Q^2 (colors). The data points are drawn at, respectively, the average generated and average reconstructed x_B in each bin. The data are generated at $s = 18 \times 275$ GeV^2 and scaled to an integrated luminosity of 10 fb^{-1}.

The statistical and systematic uncertainties are summarised in figures 6 and 7 for positive pions and in figures 8 and 9 for negative kaons. The appendix contains the corresponding figures for the other hadron species. The central value is meaningless and only has been chosen for clear visibility. The error bars represent the statistical uncertainty (scaled to an integrated luminosity of 10 fb^{-1} and accounting for beam polarisations of 70%), while the error band represents the combined systematic and statistical uncertainty. An additional 2% scale uncertainty originating from the uncertainty in the beam polarisations also

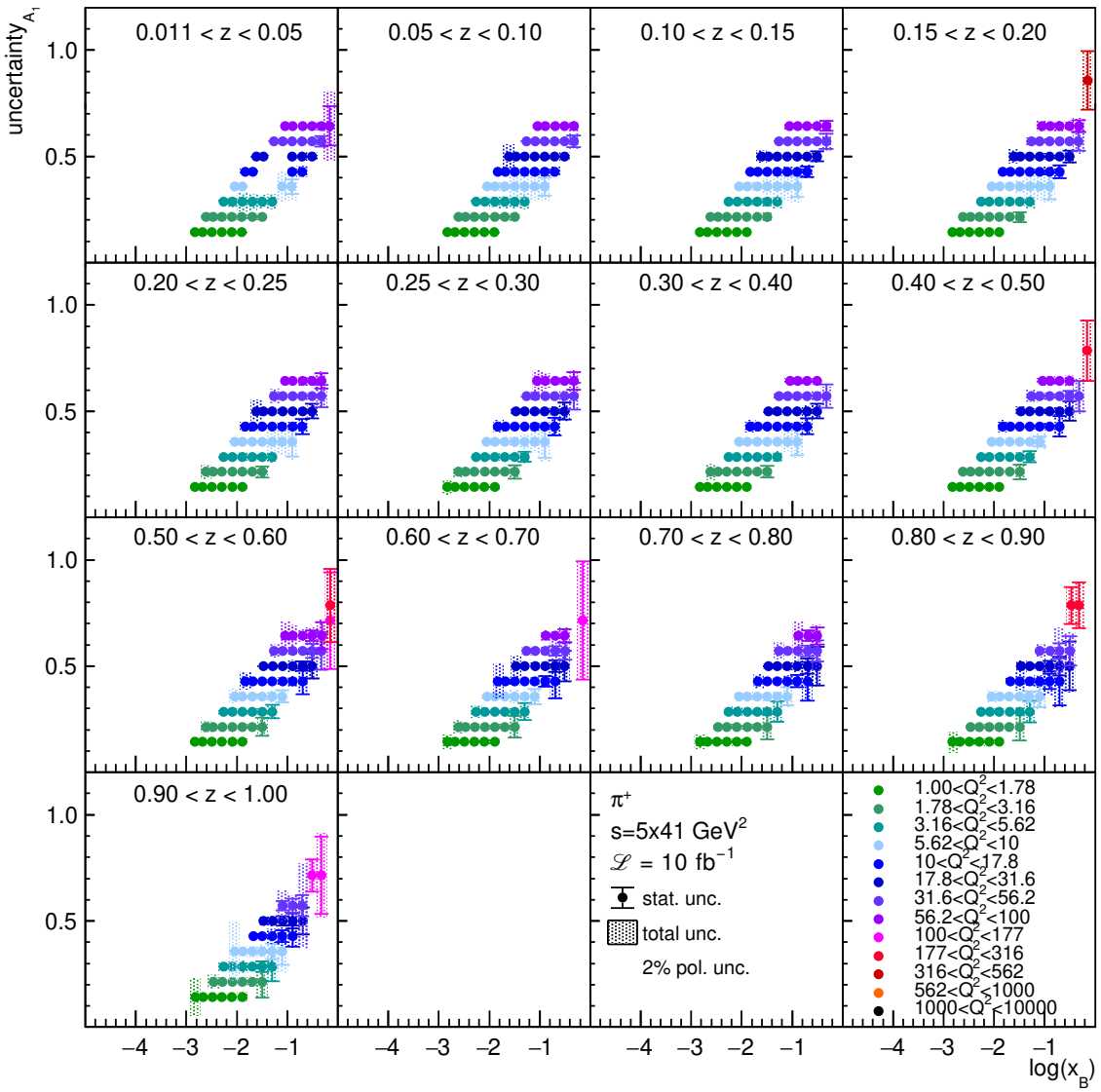

Figure 6: Statistical (error bars) and total (error bands) uncertainty for each (x_B, Q^2, z) bin, for positive-pion asymmetries collected at $s = 5 \times 41$ GeV^2. An additional global scale uncertainty of 2% accounts for the uncertainty in the beam polarisations, as indicated in the figure. The central value of the data points has no meaning.

needs to be included. On average, the systematic uncertainty is larger than the statistical uncertainty, yet, still very limited. The evaluation of the uncertainties shows that the ECCE detector design is suited to provide data with adequate precision.

The gap of data points for pions in the first z bin is due to a gap in acceptance, which stems from the support structure of the tracker in the July concept. A new layout of the tracker support system, the 'October concept' [4, 5], has been developed. The asymmetries have been evaluated for this new layout using the available, but size-limited Monte-Carlo data sample. In figure 10, the kinematic coverage and associated statistical uncertainty in the

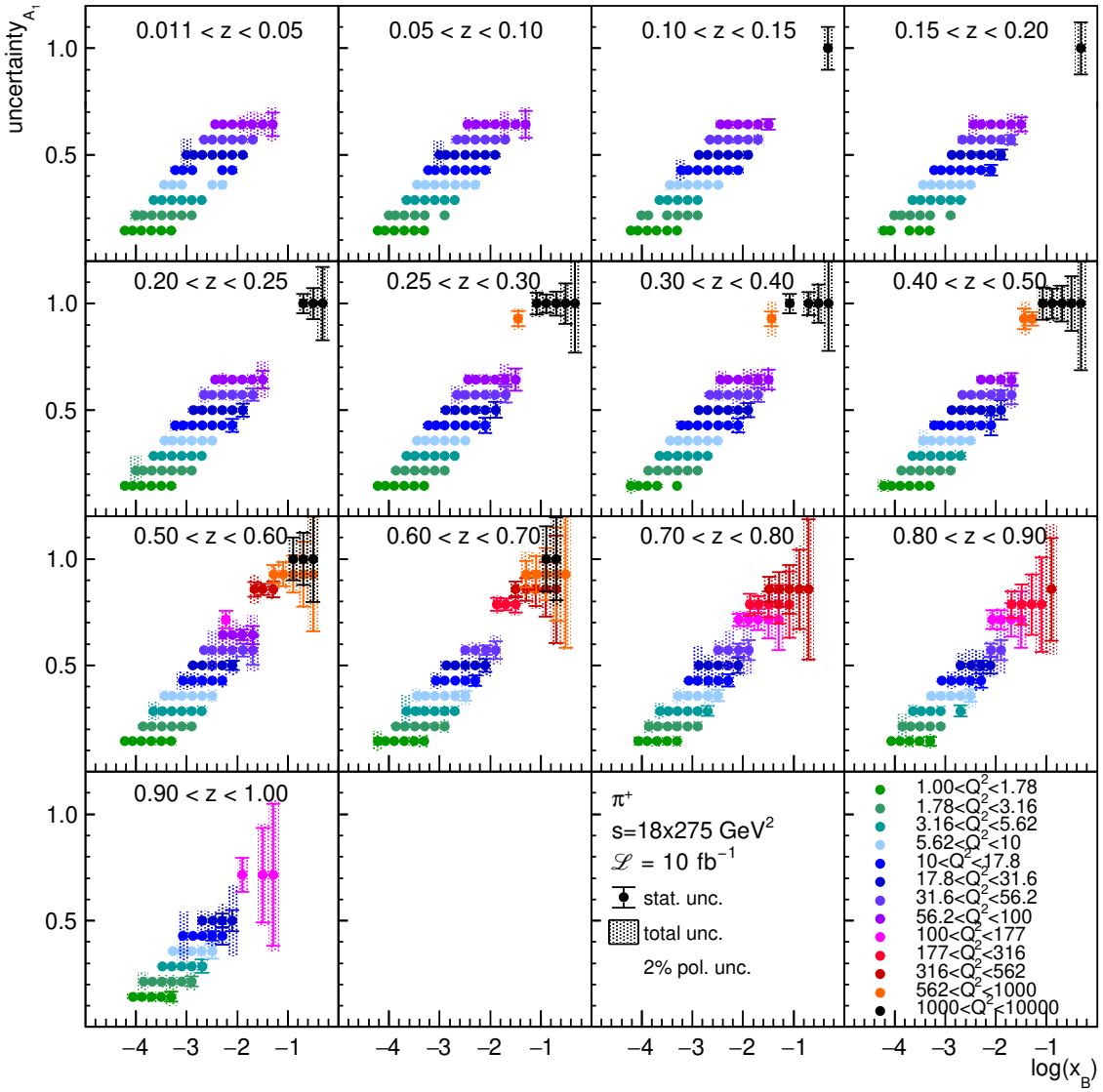

Figure 7: Statistical (error bars) and total (error bands) uncertainty for each (x_B, Q^2, z) bin, for positive-pion asymmetries collected at $s = 18 \times 275$ GeV^2. An additional global scale uncertainty of 2% accounts for the uncertainty in the beam polarisations, as indicated in the figure. The central value of the data points has no meaning.

positive-pion asymmetries for $0.011 < z < 0.05$ for the July design (left) and the October design (right) are presented. As can be seen, the new tracker support structure closes the gap in acceptance.

Finally, figures 11 and 12 illustrate the asymmetry that would be obtained after an unfolding procedure on the asymmetry measured with the ECCE detector, for 10 fb^{-1} of data collected at $s = 5 \times 41$ GeV^2 and $s = 18 \times 275$ GeV^2, respectively[4], for the range

[4]In practice, the central values of the reconstructed asymmetries have been replaced here by those of the generated ones, for the kinematic bins for which an asymmetry is reconstructed.

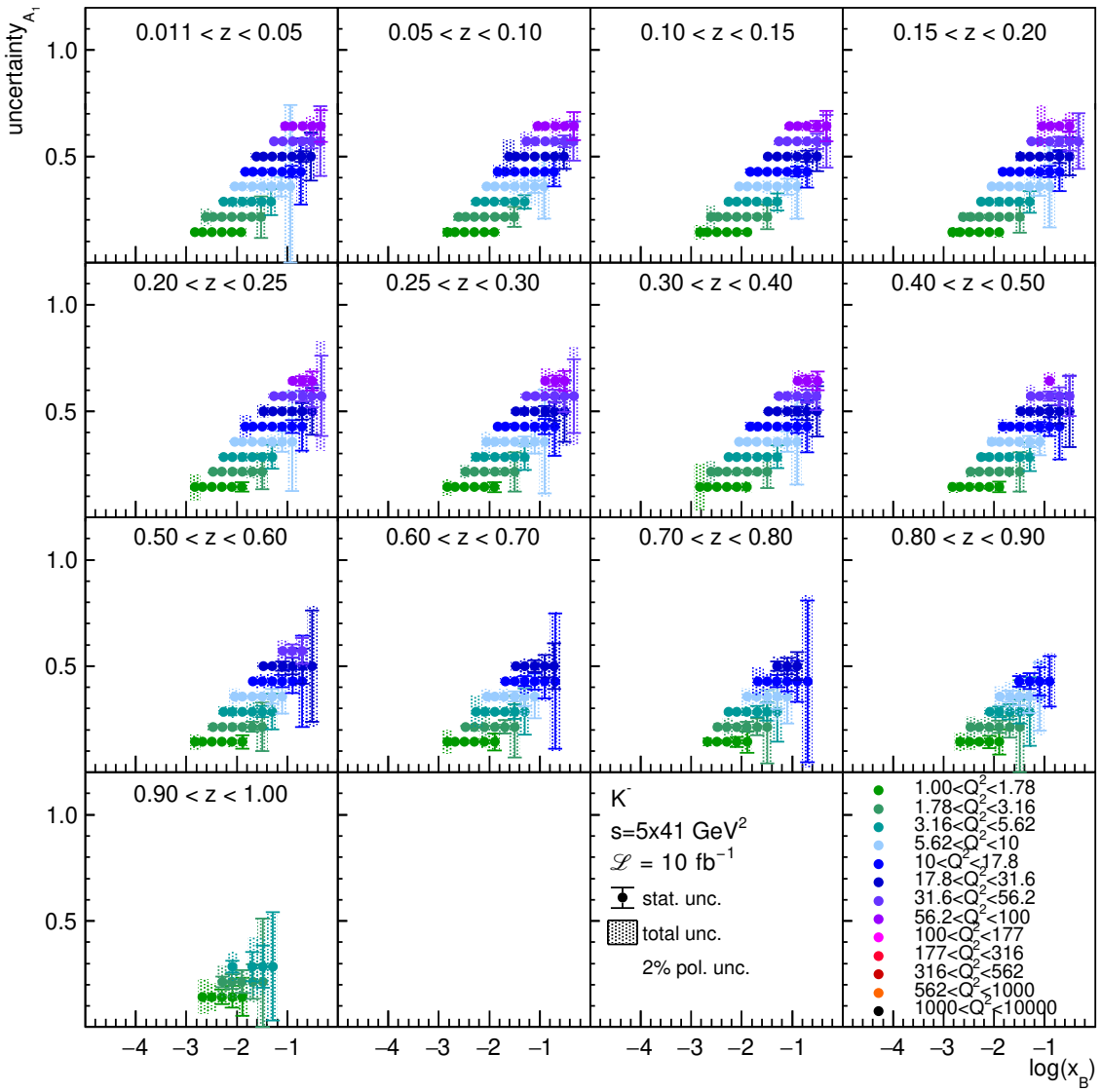

Figure 8: Statistical (error bars) and total (error bands) uncertainty for each (x_B, Q^2, z) bin, for negative-kaon asymmetries collected at $s = 5 \times 41$ GeV^2. An additional global scale uncertainty of 2% accounts for the uncertainty in the beam polarisations, as indicated in the figure. The central value of the data points has no meaning.

10.0 GeV^2 $< Q^2 <$ 17.8 GeV^2 and three ranges in z. The systematic uncertainties, evaluated as described above, are indicated as well. These figures also again clearly illustrate the complementarity between data collected at the two centre-of-mass energies and their reach in x_B for a fixed range in z.

As stated previously, the here performed studies are based on simulations with the field strength of the ECCE superconducting solenoid set to 1.4 T. An alternative configuration, where the field strength is set to 3.0 T has also been considered. The influence of the higher magnetic field strength is illustrated in figures 13 and 14. As figures 6–9, figure 13

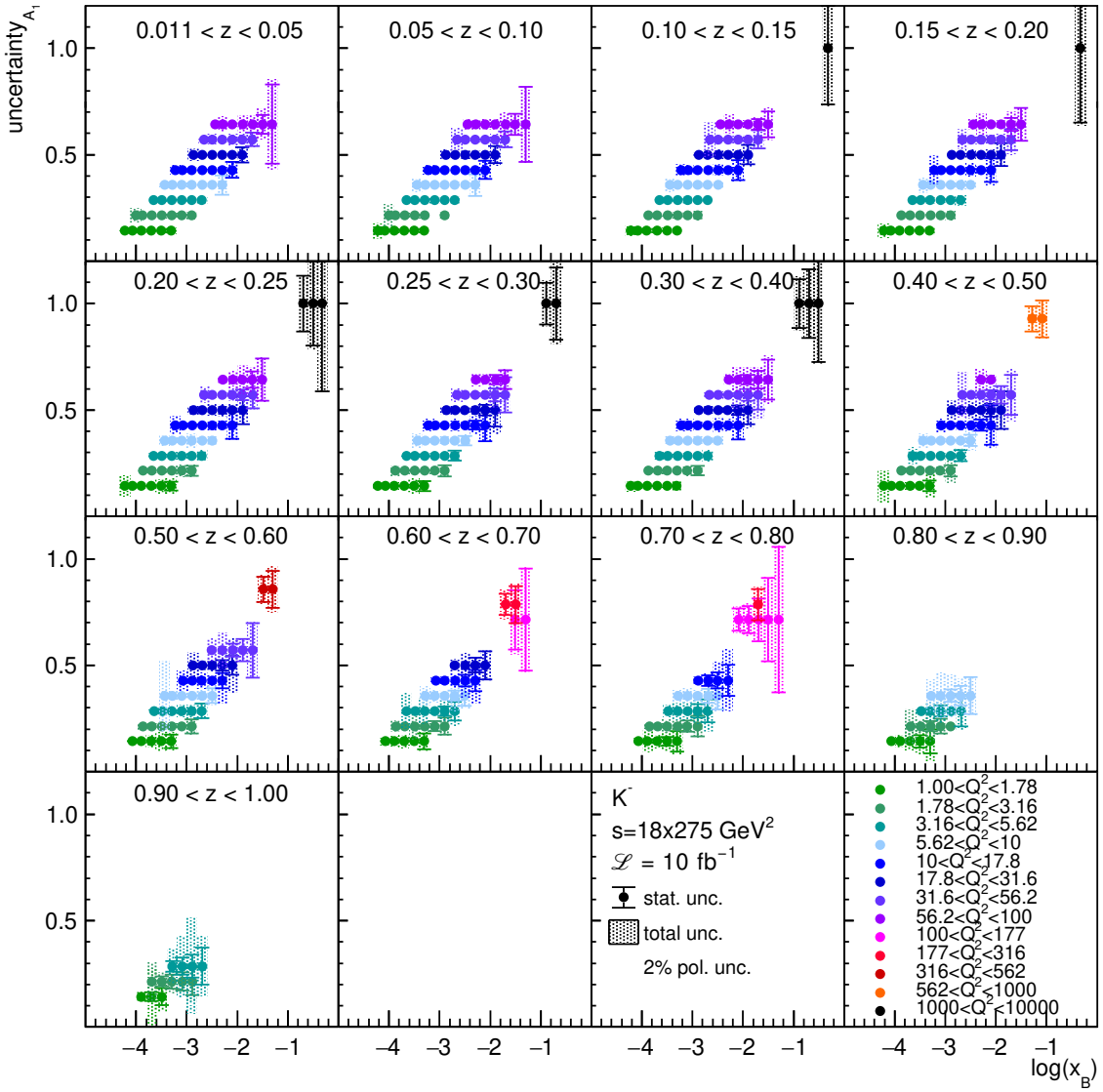

Figure 9: Statistical (error bars) and total (error bands) uncertainty for each (x_B, Q^2, z) bin, for negative-kaon asymmetries collected at $s = 18 \times 275$ GeV^2. An additional global scale uncertainty of 2% accounts for the uncertainty in the beam polarisations, as indicated in the figure. The central value of the data points has no meaning.

shows the uncertainties in the A_1 asymmetry as a function of the kinematic coverage in x_B (x-axis) and Q^2 (colors). Here, the results for $s = 18 \times 275$ GeV^2 and one bin in hadron fractional energy $0.10 < z < 0.15$ are shown. Comparing the 1.4 T setting (first panel) and the 3.0 T setting (second panel), it can be seen that the 3.0 T configuration allows for a similar kinematic coverage as the 1.4 T configuration. The observed behaviour is similar in all of the z bins. Additional information is provided in figure 14, which shows the ratio of the statistical uncertainties in the asymmetry for the 1.4 T and 3.0 T configuration for $0.10 < z < 0.15$ (left) and $0.60 < z < 0.70$ (middle). The low-z bin is in general populated by low-energetic hadrons. Since these are more likely to be deviated out of the detector

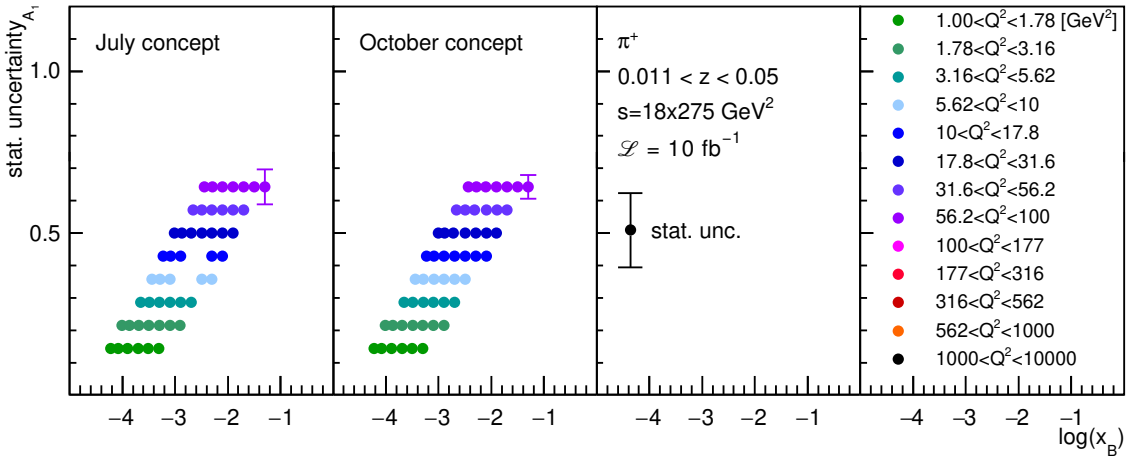

Figure 10: Statistical uncertainty for each (x_B, Q^2) bin and for $0.011 < z < 0.04$, for positive-pion asymmetries collected at $s = 18 \times 275$ GeV^2. The central value of the data points has no meaning. The panel on the left shows the situation for the July design, while that in the middle shows the situation for the October design.

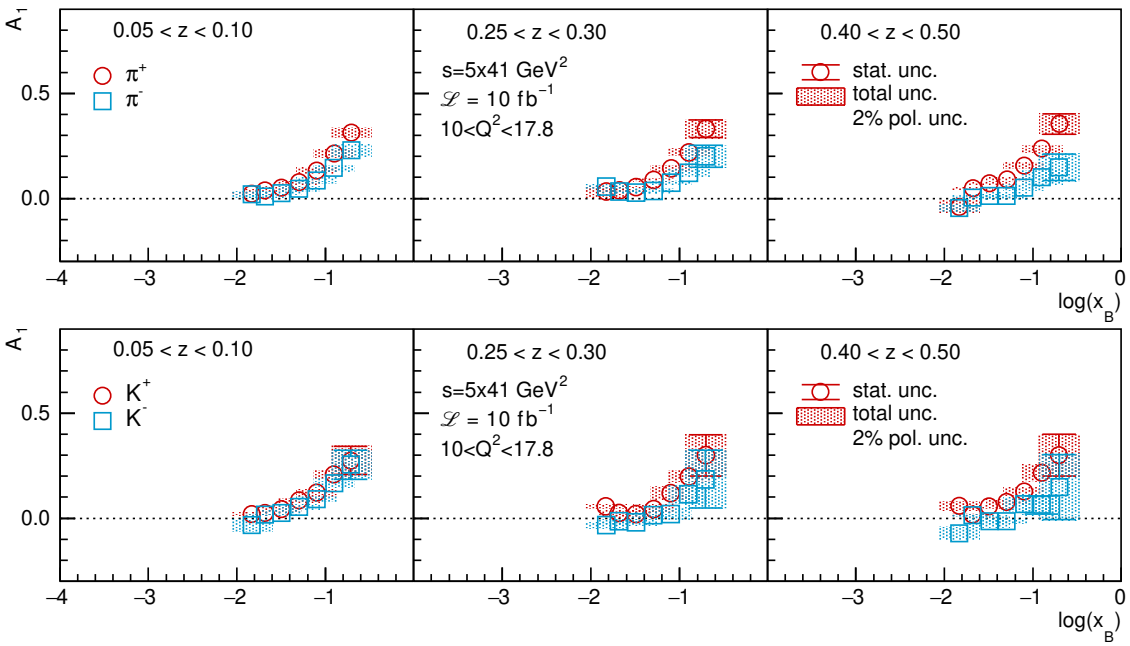

Figure 11: 'Unfolded' pion (upper panel) and kaon (lower panel) asymmetries as a function of x_B for 10.0 GeV^2 $< Q^2 <$ 17.8 GeV^2 and three ranges in z, obtained from data at $s = 5 \times 41$ GeV^2 and for an integrated luminosity of 10 fb^{-1}.

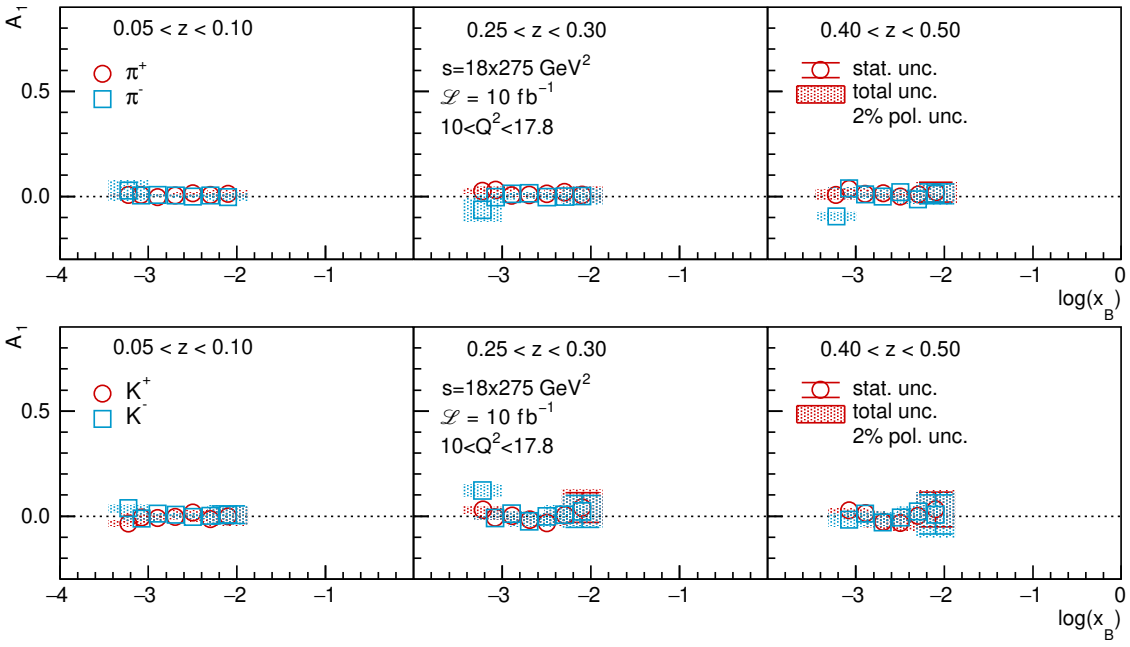

Figure 12: 'Unfolded' pion (upper panel) and kaon (lower panel) asymmetries as a function of x_B for 10.0 GeV^2 $< Q^2 <$ 17.8 GeV^2 and three ranges in z, obtained from data at $s = 18 \times 275$ GeV^2 and for an integrated luminosity of 10 fb^{-1}.

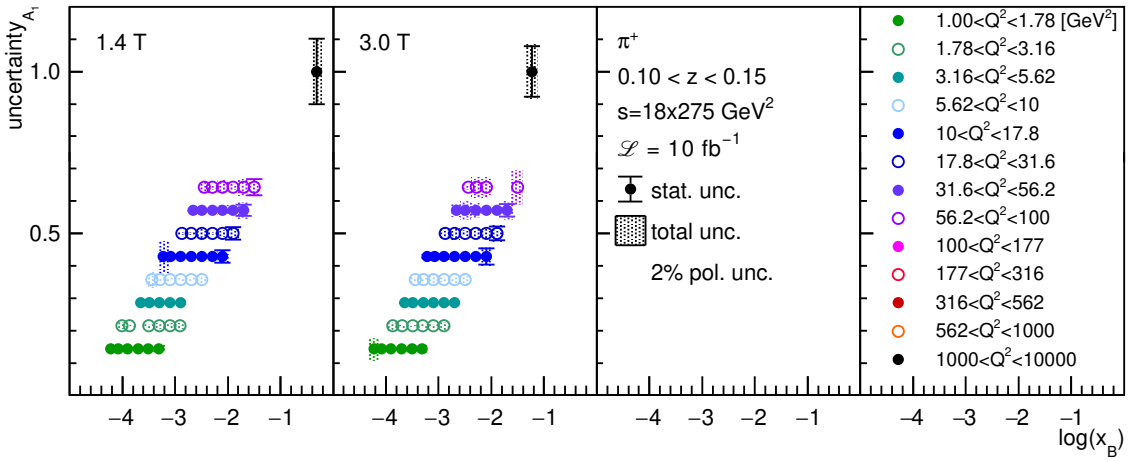

Figure 13: Statistical (error bars) and total (error bands) uncertainty for each (x_B, Q^2) bin and $0.10 < z < 0.15$, for positive-pion asymmetries collected at $s = 18 \times 275$ GeV^2. An additional global scale uncertainty of 2% accounts for the uncertainty in the beam polarisations, as indicated in the figure. The central value of the data points has no meaning. The first panel shows the kinematic coverage and related uncertainties with the 1.4 T magnetic configuration, while the second panel shows the 3.0 T configuration.

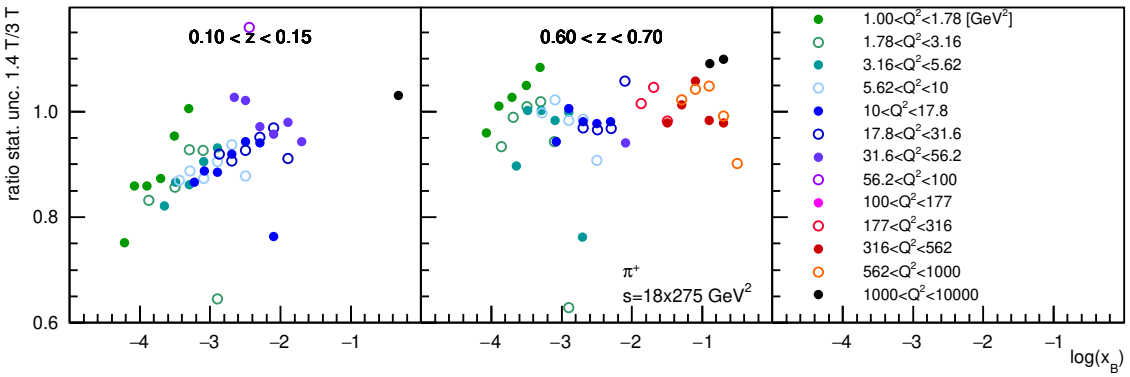

Figure 14: Ratio of the statistical uncertainties for positive-pion asymmetries collected at $s = 18 \times 275$ GeV^2 with the 1.4 T and 3.0 T configurations, as a function of x_B (x axis) and Q^2 (color), for $0.10 < z < 0.15$ (left) and $0.60 < z < 0.70$ (middle).

acceptance by higher magnetic fields, the ratio of the uncertainties is on average below 1.0 for this low-z bin. A higher-z region, depicted in the middle panel, illustrates the fact that the higher-energetic hadrons are less deviated by a higher magnetic field, resulting in an average statistical-uncertainty ratio centered around 1. An increase of the ratio as a function of x_B is observed for fixed values of Q^2, a trend most clearly observed in the lower z region, though also visible for higher z values. This means that the 3.0 T configuration allows for a better coverage at larger values of x_B for fixed Q^2, apart for the highest x_B bin at fixed Q^2, where a drop of the ratio, likely linked to the lower cut on y and finite resolution, is observed.

4 Evaluation of the helicity distributions

The impact of the ECCE data on the helicity distributions is evaluated for the energy configurations 5×41 GeV^2 and 18×275 GeV^2. The procedure follows that adopted in Ref. [13], where the DSSV14 helicity distributions are used in order to generate the observables, while the statistical and systematic uncertainties described in the previous section are taken for the uncertainty estimate.

As starting point, a new DSSV14 set of helicity distributions extracted from simulated EIC data at 45 GeV^2 and taken from Ref. [13] is used. From this new set of helicity distributions, new sets of helicity distributions are generated. The latter are obtained by fitting the simulated EIC data at 45 GeV^2 that has been smeared according to its statistical and systematic uncertainty. Following this, the obtained sets of helicity distributions are used to construct the double-spin asymmetry, where each set is weighted according to its degree of agreement with the asymmetries evaluated at 5×41 GeV^2 or 18×275 GeV^2, as presented in the previous section. As such, one obtains a new set of helicity distributions that best describes the asymmetry that is evaluated together with the associated uncertainty. Note that in principle one could start from the original set of DSSV14 helicity distributions.

However, given the high precision of the EIC data and its partially new phase-space coverage, reweighting the original DSSV14 helicity distributions would result in a very limited number of newly generated sets of helicity distributions in agreement with the ECCE data, and as a result it would compromise the statistical accuracy.

The evaluated impact of the ECCE data at 5×41 GeV^2 and 18×275 GeV^2 is visible in the figures **??**. As can be seen, the impact on the sea-quark helicity distributions substantial.

5 Summary and outlook

The evaluation of the measurement of double-spin asymmetries in semi-inclusive DIS using the ECCE detector has been presented for pion and kaon production. The study shows that the ECCE design is well suited for the measurement of such asymmetries and for the subsequent extraction of parton helicity distributions. First, the resolution of the ECCE detector is such that the smearing of kinematic variables is limited. Secondly, the design provides a good acceptance, allowing for the measurement of asymmetries that already without corrections reflect closely the generated asymmetries. Furthermore, the envisioned detector provides a broad kinematic coverage in x_B, Q^2, and z, aided by the possibility to vary the beam energies. In turn, the broad kinematic coverage, down to $x_B = 10^{-4}$, and a high precision are essential to constrain the helicity distributions, in particular the sea-quark and gluon helicity distributions at low x_B, which so far remain largely unconstrained.

Acknowledgments

A Appendix

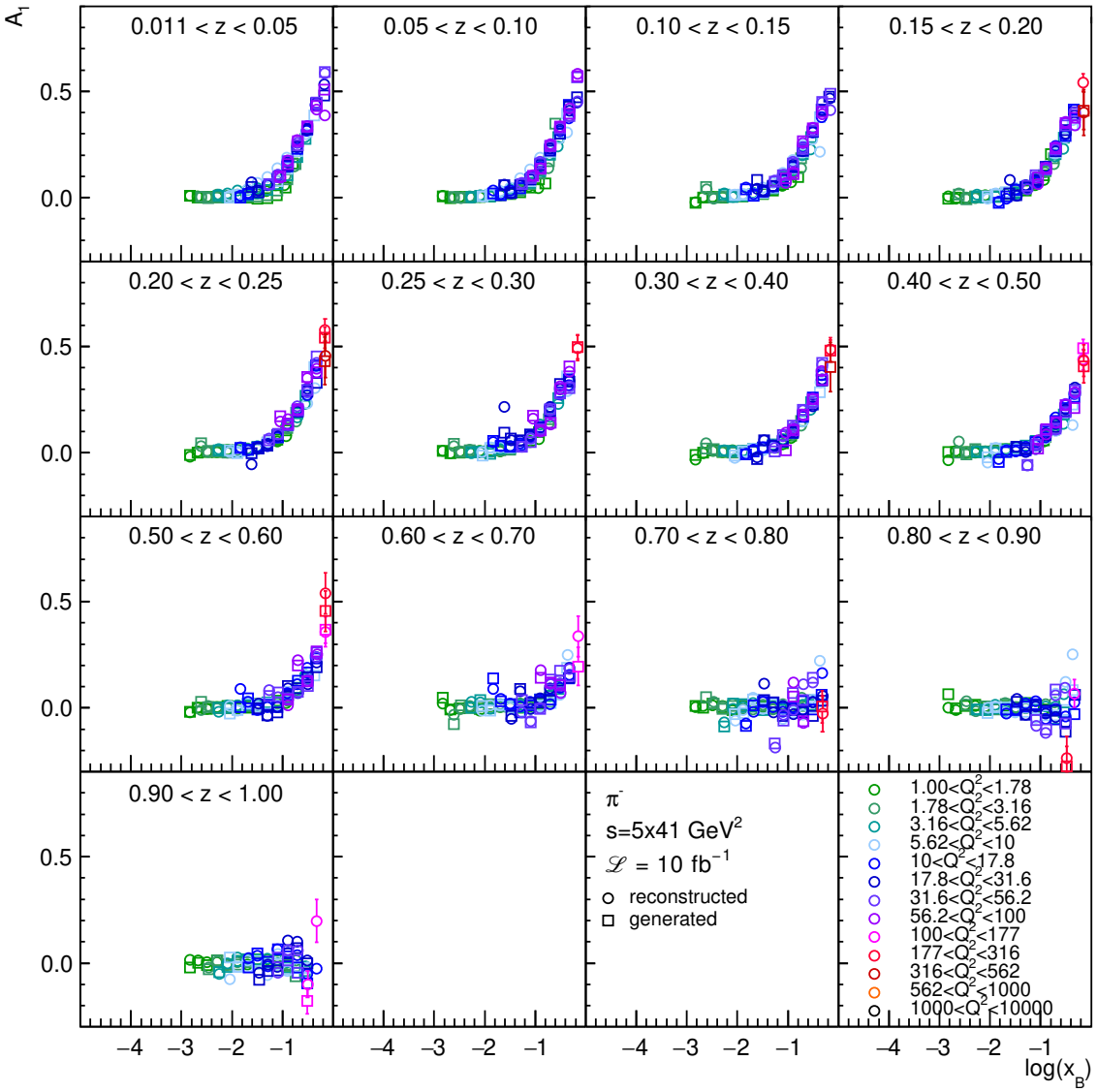

Figure 15: Generated (squares) and reconstructed (circles) double-spin asymmetries with $D(y) = 1$ for negative pions, as a function of x_B and for different ranges in z (panels) and Q^2 (colors). The data points are drawn at, respectively, the average generated and average reconstructed x_B in each bin. The data are generated at $s = 5 \times 41$ GeV^2 and scaled to an integrated luminosity of 10 fb^{-1}.

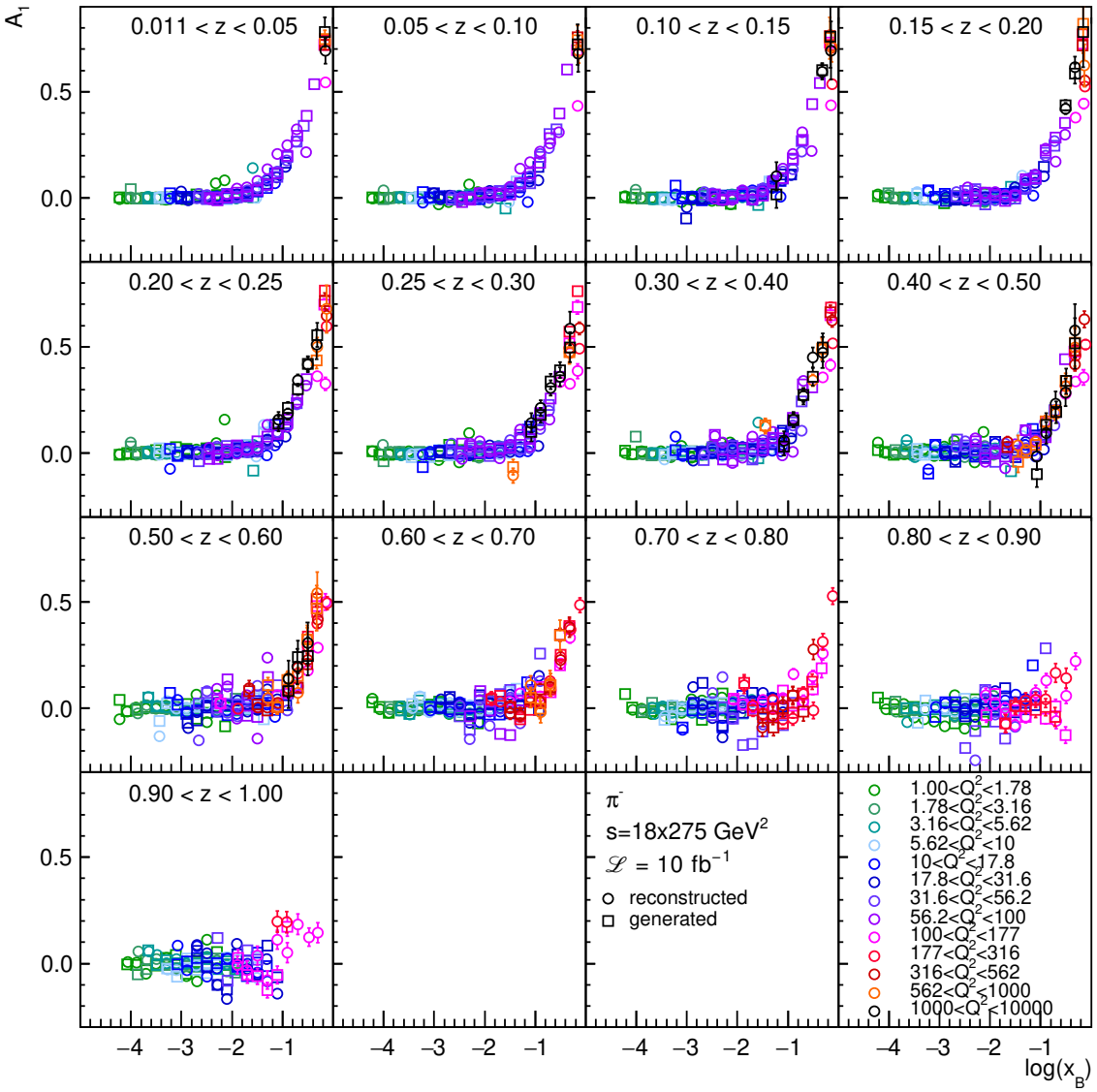

Figure 16: Generated (squares) and reconstructed (circles) double-spin asymmetries with $D(y) = 1$ for negative pions, as a function of x_B and for different ranges in z (panels) and Q^2 (colors). The data points are drawn at, respectively, the average generated and average reconstructed x_B in each bin. The data are generated at $s = 18 \times 275$ GeV^2 and scaled to an integrated luminosity of 10 fb^{-1}.

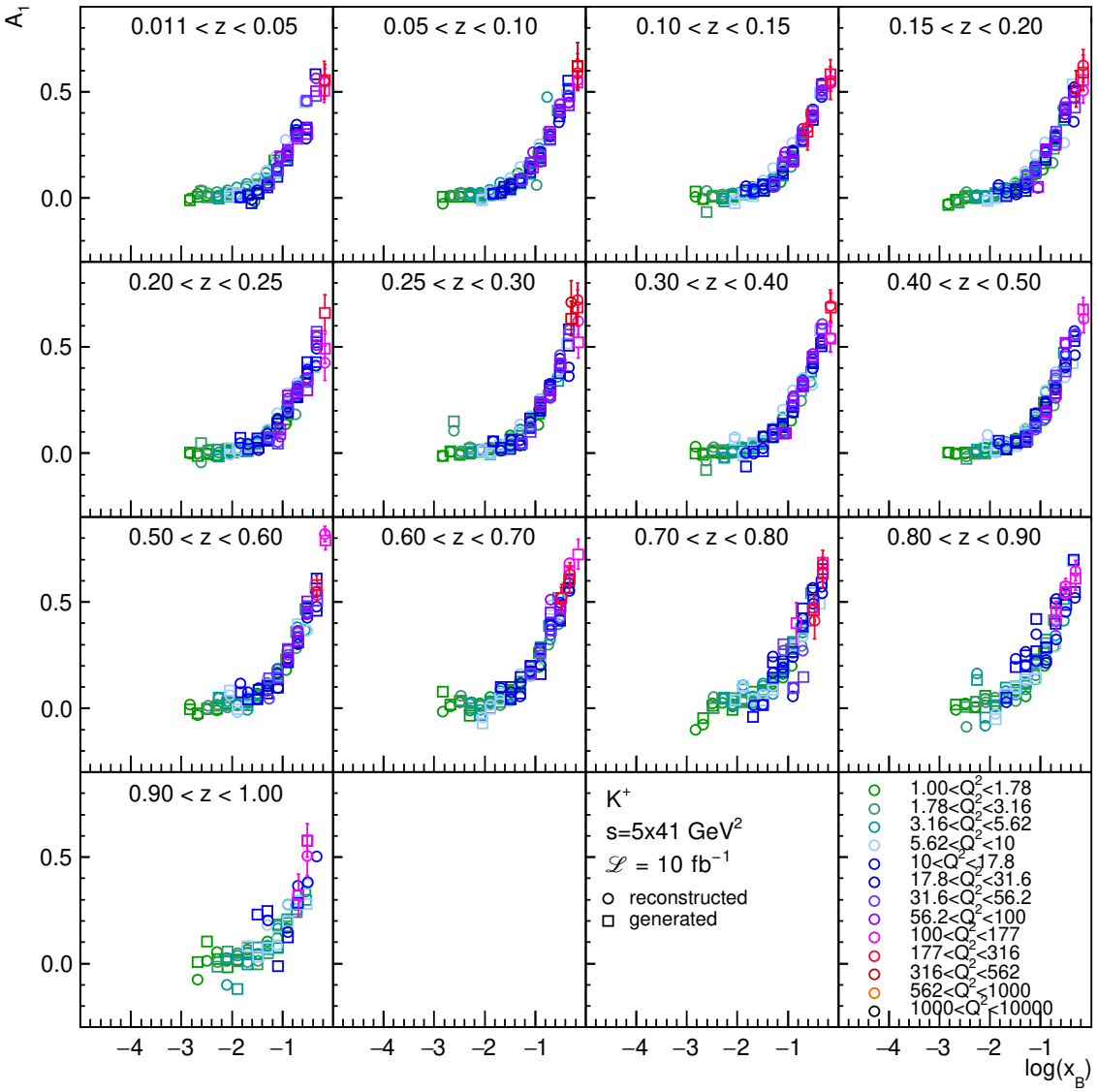

Figure 17: Generated (squares) and reconstructed (circles) double-spin asymmetries with $D(y) = 1$ for positive kaons, as a function of x_B and for different ranges in z (panels) and Q^2 (colors). The data points are drawn at, respectively, the average generated and average reconstructed x_B in each bin. The data are generated at $s = 5 \times 41$ GeV^2 and scaled to an integrated luminosity of 10 fb^{-1}.

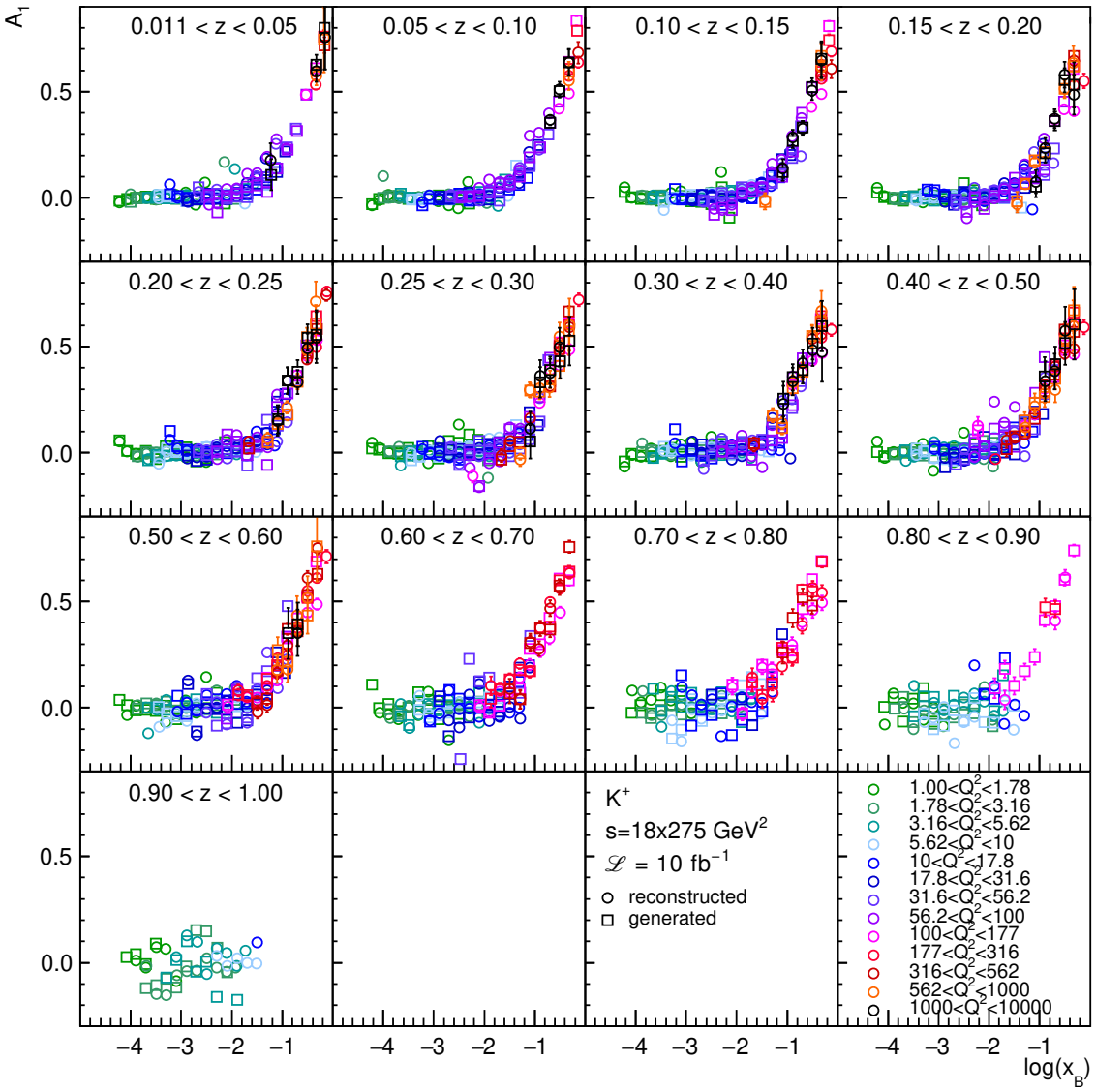

Figure 18: Generated (squares) and reconstructed (circles) double-spin asymmetries with $D(y) = 1$ for positive kaons, as a function of x_B and for different ranges in z (panels) and Q^2 (colors). The data points are drawn at, respectively, the average generated and average reconstructed x_B in each bin. The data are generated at $s = 18 \times 275$ GeV^2 and scaled to an integrated luminosity of 10 fb^{-1}.

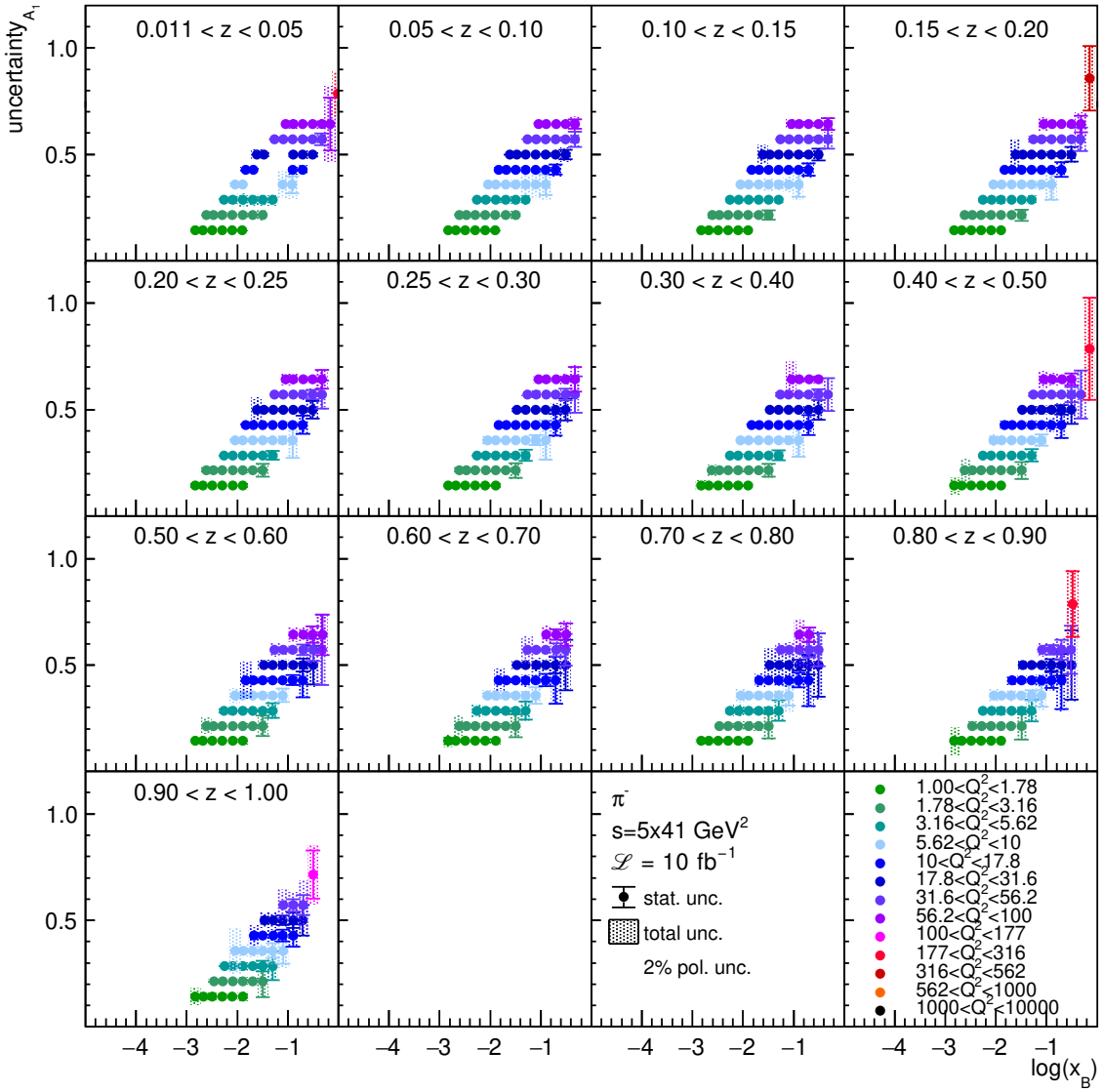

Figure 19: Statistical (error bars) and total (error bands) uncertainty for each (x_B, Q^2, z) bin, for negative-pion asymmetries collected at $s = 5 \times 41$ GeV^2. An additional global scale uncertainty of 2% accounts for the uncertainty in the beam polarisations, as indicated in the figure. The central value of the data points has no meaning.

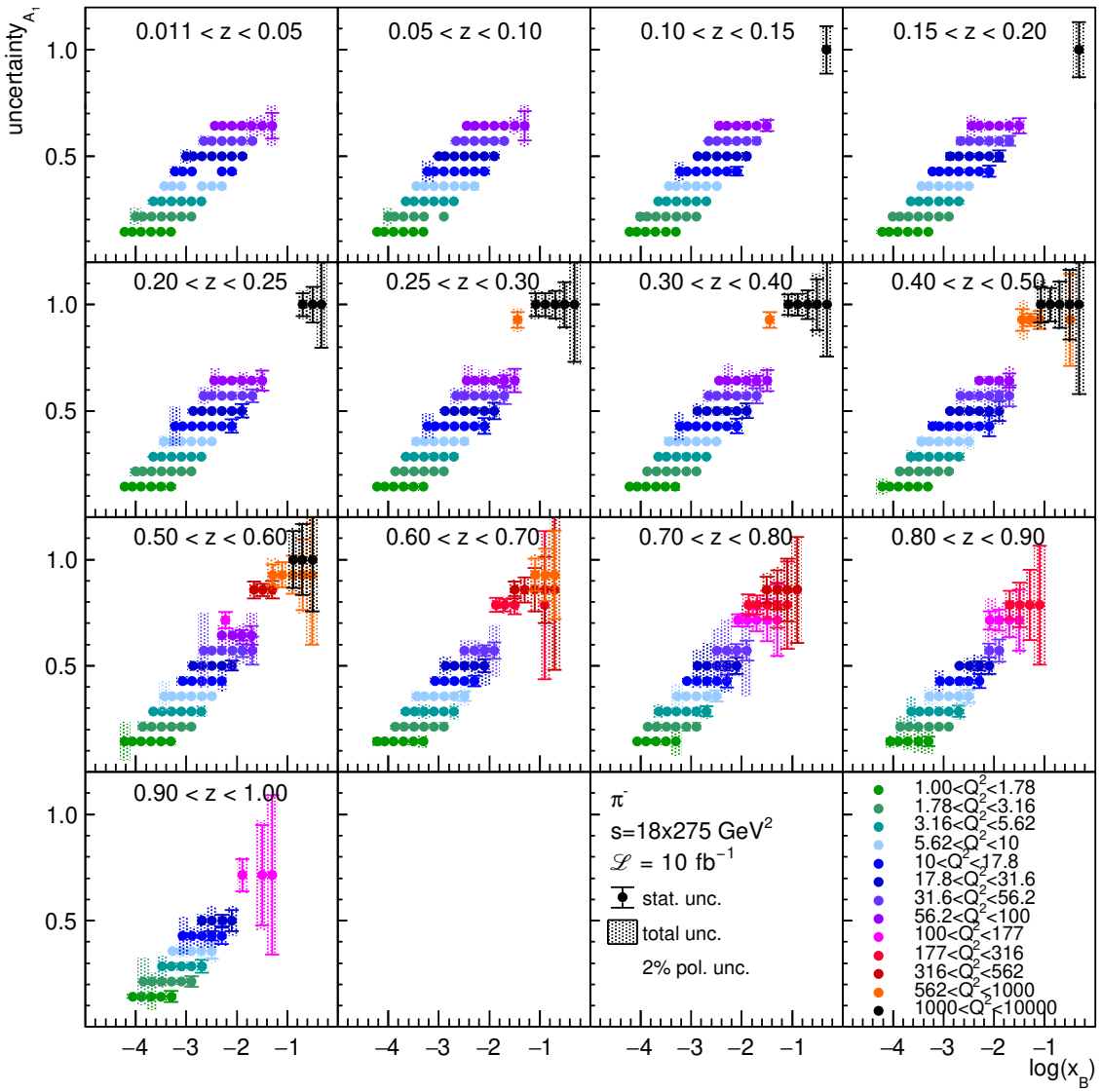

Figure 20: Statistical (error bars) and total (error bands) uncertainty for each (x_B, Q^2, z) bin, for negative-pion asymmetries collected at $s = 18 \times 275$ GeV^2. An additional global scale uncertainty of 2% accounts for the uncertainty in the beam polarisations, as indicated in the figure. The central value of the data points has no meaning.

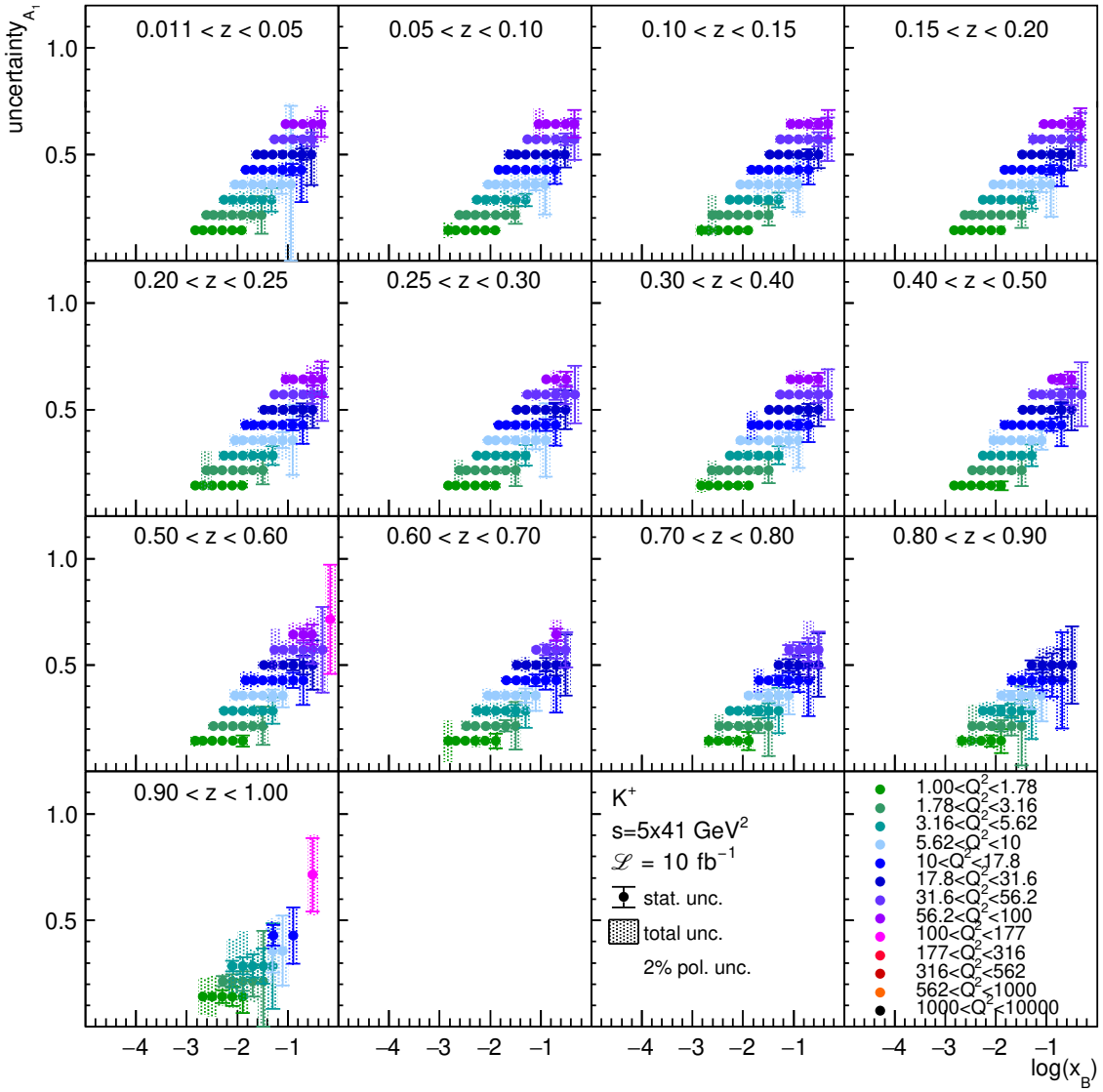

Figure 21: Statistical (error bars) and total (error bands) uncertainty for each (x_B, Q^2, z) bin, for positive-kaon asymmetries collected at $s = 5 \times 41$ GeV^2. An additional global scale uncertainty of 2% accounts for the uncertainty in the beam polarisations, as indicated in the figure. The central value of the data points has no meaning.

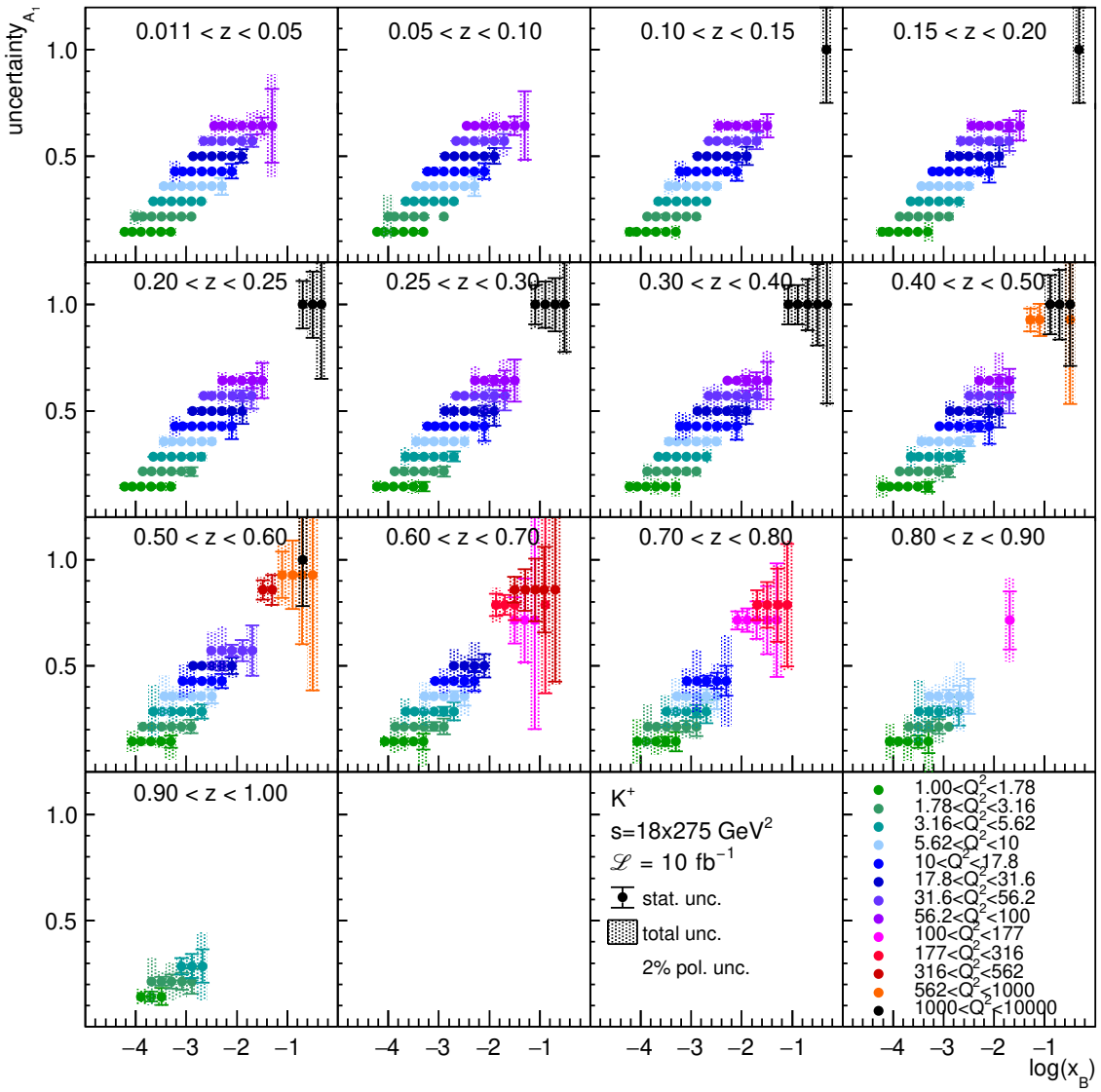

Figure 22: Statistical (error bars) and total (error bands) uncertainty for each (x_B, Q^2, z) bin, for positive-kaon asymmetries collected at $s = 18 \times 275$ GeV^2. An additional global scale uncertainty of 2% accounts for the uncertainty in the beam polarisations, as indicated in the figure. The central value of the data points has no meaning.

References

[1] Daniel de Florian, Rodolfo Sassot, Marco Stratmann, and Werner Vogelsang. Evidence for polarization of gluons in the proton. *Phys. Rev. Lett.*, 113:012001, Jul 2014. URL: https://link.aps.org/doi/10.1103/PhysRevLett.113.012001, doi:10.1103/PhysRevLett.113.012001. 1, 2

[2] Torbjorn Sjostrand, Stephen Mrenna, and Peter Z. Skands. PYTHIA 6.4 Physics and Manual. *JHEP*, 05:026, 2006. arXiv:hep-ph/0603175, doi:10.1088/1126-6708/2006/05/026. 2

[3] R. Abdul Khalek et al. Science Requirements and Detector Concepts for the Electron-Ion Collider: EIC Yellow Report. 3 2021. arXiv:2103.05419. 2

[4] ECCE Computing Plan, 2021. https://TBD[TBD]. 2, 3

[5] ECCE Software and Simulation for detector proposal, 2021. https://TBD[TBD]. 2, 3

[6] K. Abe et al. Measurements of R = σ(L) / σ(T) for 0.03 $<$ x $<$ 0.1 and fit to world data. *Phys. Lett. B*, 452:194–200, 1999. arXiv:hep-ex/9808028, doi:10.1016/S0370-2693(99)00244-0. 2

[7] Daniel de Florian, Gonzalo Agustín Lucero, Rodolfo Sassot, Marco Stratmann, and Werner Vogelsang. Monte carlo sampling variant of the dssv14 set of helicity parton densities. *Phys. Rev. D*, 100:114027, Dec 2019. URL: https://link.aps.org/doi/10.1103/PhysRevD.100.114027, doi:10.1103/PhysRevD.100.114027. 2

[8] Daniel de Florian, R. Sassot, Manuel Epele, Roger J. Hernández-Pinto, and Marco Stratmann. Parton-to-pion fragmentation reloaded. *Phys. Rev. D*, 91:014035, Jan 2015. URL: https://link.aps.org/doi/10.1103/PhysRevD.91.014035, doi:10.1103/PhysRevD.91.014035. 2

[9] D. de Florian, M. Epele, R. J. Hernandez-Pinto, R. Sassot, and M. Stratmann. Parton-to-Kaon Fragmentation Revisited. *Phys. Rev. D*, 95(9):094019, 2017. arXiv:1702.06353, doi:10.1103/PhysRevD.95.094019. 2

[10] Richard D. Ball et al. Parton distributions for the LHC Run II. *JHEP*, 04:040, 2015. arXiv:1410.8849, doi:10.1007/JHEP04(2015)040. 2

[11] Andy Buckley, James Ferrando, Stephen Lloyd, Karl Nordström, Ben Page, Martin Rüfenacht, Marek Schönherr, and Graeme Watt. LHAPDF6: parton density access in the LHC precision era. *Eur. Phys. J. C*, 75:132, 2015. arXiv:1412.7420, doi:10.1140/epjc/s10052-015-3318-8. 2

[12] D. de Florian, M. Stratmann, and W. Vogelsang. QCD analysis of unpolarized and polarized Lambda baryon production in leading and next-to-leading order. *Phys. Rev. D*, 57:5811–5824, 1998. arXiv:hep-ph/9711387, doi:10.1103/PhysRevD.57.5811. 2

[13] Ignacio Borsa, Gonzalo Lucero, Rodolfo Sassot, Elke C. Aschenauer, and Ana S. Nunes. Revisiting helicity parton distributions at a future electron-ion collider. *Phys. Rev. D*, 102:094018, Nov 2020. URL: https://link.aps.org/doi/10.1103/PhysRevD.102.094018, doi:10.1103/PhysRevD.102.094018. 4

ECCE consortium

J. K. Adkins[42], Y. Akiba[59], A. Albataineh[79], M. Amaryan[53], I. C. Arsene[84], J. Bae[69], X. Bai[92], M. Bashkanov[101], R. Bellwied[77], F. Benmokhtar[15], J. C. Bernauer[62, 63, 64], F. Bock[55], W. Boeglin[17], M. Borysova[97], E. Brash[11], P. Brindza[33], W. J. Briscoe[21], M. Brooks[38], S. Bueltmann[53], M. H. S. Bukhari[31], A. Bylinkin[79], R. Capobianco[76], W.-C. Chang[2], Y. Cheon[67], K. Chen[8], K.-F. Chen[52], K.-Y. Cheng[46], M. Chiu[5], T. Chujo[89], Z. Citron[4], E. Cline[62, 63], E. Cohen[50], T. Cormier[55], Y. Corrales Morales[38], C. Cotton[92], C. Crawford[80], S. Creekmore[55], C.Cuevas[33], J. Cunningham[55], G. David[5], C. T. Dean[38], M. Demarteau[55], S. Diehl[76], N. Doshita[99], R. Dupré[25], J. M. Durham[38], R. Dzhygadlo[20], R. Ehlers[55], L. El Fassi[44], A. Emmert[92], R. Ent[33], C. Fanelli[43], R. Fatemi[80], S. Fegan[101], M. Finger[9], M. Finger Jr.[9], J. Frantz[53], M. Friedman[24], I. Friscic[102], D. Gangadharan[77], S. Gardner[19], K. Gates[19], F. Geurts[58], R. Gilman[60], D. Glazier[19], E. Glimos[55], Y. Goto[59], N. Grau[3], S. V. Greene[93], A. Q. Guo[26], L. Guo[17], S. K. Ha[100], J. Haggerty[5], T. Hayward[76], X. He[18], O. Hen[43], D. Higinbotham[33], M. Hoballah[25], P.-h. J. Hsu[51], J. Huang[5], G. Huber[85], A. Hutson[77], K. Y. Hwang[100], C. Hyde[53], M. Inaba[73], T. Iwata[99], H.-S. Jo[37], K. Joo[76], N. Kalantarians[95], K. Kawade[68], S. Kay[85], A. Kim[76], B. Kim[69], C. Kim[57], M. Kim[59], Y. Kim[57], Y. Kim[67], E. Kistenev[5], V. Klimenko[76], S. H. Ko[66], I. Korover[43], W. Korsch[80], G. Krintiras[79], S. Kuhn[53], C.-M. Kuo[46], T. Kutz[43], J. Lajoie[28], D. Lawrence[33], S. Lebedev[28], J. S. H. Lee[66], S. W. Lee[37], Y.-J. Lee[43], W. Li[58], W. Li[62, 63, 98], X. Li[10], X. Li[38], Y. T. Liang[26], S. Lim[57], C.-h. Lin[2], D. X. Lin[26], K. Liu[38], M. X. Liu[38], K. Livingston[19], N. Liyanage[92], W. J. Llope[96], C. Loizides[55], E. Long[83], R.-S. Lu[52], Z. Lu[10], W. Lynch[101], D. Marchand[25], M. Marcisovsky[14], P. Markowitz[17], P. McGaughey[38], M. Mihovilovic[81], R. G. Milner[43], A. Milov[97], Y. Miyachi[99], P. Monaghan[11], R. Montgomery[19], D. Morrison[5], C. Munoz Camacho[25], M. Murray[79], K. Nagai[38], J. Nagle[74], I. Nakagawa[59], C. Nattrass[90], D. Nguyen[33], S. Niccolai[25], R. Nouicer[5], G. Nukazuka[59], M. Nycz[92], V. A. Okorokov[49], S. Orešić[85], J. Osborn[55], C. O'Shaughnessy[38], S. Paganis[52], Z Papandreou[85], S. Pate[48], M. Patel[28], C. Paus[43], G. Penman[19], M. G. Perdekamp[78], D. V. Perepelitsa[74], H. Periera da Costa[38], K. Peters[20], W. Phelps[11], E. Piasetzky[70], C. Pinkenburg[5], I. Prochazka[9], T. Protzman[40], M. Purschke[5], J. Putschke[96], J. R. Pybus[43], R. Rajput-Ghoshal[33], J. Rasson[55], B. Raue[17], K. Read[55], K. Røed[84], R. Reed[40], J. Reinhold[17], E. L. Renner[38], J. Richards[76], C. Riedl[78], T. Rinn[5], J. Roche[53], G. M. Roland[43], G. Ron[24], M. Rosati[28], C. Royon[79], J. Ryu[57], S. Salur[60], N. Santiesteban[43], R. Santos[76], M. Sarsour[18], J. Schambach[55], A. Schmidt[21], N. Schmidt[55], C. Schwarz[20], J. Schwiening[20], R. Seidl[59], A. Sickles[78], P. Simmerling[76], S. Sirca[81], D. Sharma[18], Z. Shi[38], T.-A. Shibata[47], C.-W. Shih[46], S. Shimizu[59], U. Shrestha[76], K. Slifer[83], K. Smith[38], R. Soltz[41], W. Sondheim[38], J. Song[10], J. Song[57], I. I. Strakovsky[21], P. Steinberg[5], J. Stevens[98], J. Strube[56], P. Sun[10], X. Sun[8], K. Suresh[85], W.-C. Tang[46], S. Tapia Araya[28], S. Tarafdar[93], L. Teodorescu[6], A. Timmins[77], L. Tomasek[14], N. Trotta[76], T. S. Tveter[84], E. Umaka[28], A. Usman[85], H. W. van Hecke[38], J. Velkovska[93], E. Voutier[25], P.K. Wang[25], Q. Wang[79], Y. Wang[8], Y. Wang[72], D. P. Watts[101], L. Weinstein[53], M. Williams[43], C.-P. Wong[38], L. Wood[56], M. H. Wood[7], C. Woody[5], B. Wyslouch[43], Z. Xiao[72], Y. Yamazaki[35], Y. Yang[45], Z. Ye[72], H. D. Yoo[100], M. Yurov[38], N. Zachariou[101], W.A. Zajc[12], J. Zhang[92], Y. Zhang[72], Y. X. Zhao[26], X. Zheng[92], P. Zhuang[72],

[82], [32], [36], [71], [75], [87], [88], [91], [94], [1], [13], [16], [22], [23], [27], [29], [30], [34], [39], [61], [65], and [103]

[1]

[2]*Institute of Physics, Academia Sinica, Taipei, Taiwan*
[3]*Augustana University, Sioux Falls, SD, USA*
[4]

[5]*Brookhaven National Laboratory, Upton, NY, USA*
[6]*Brunel University London, Uxbridge, UK*
[7]*Canisius College, Buffalo, NY, USA*
[8]*Central China Normal University, Wuhan, China*
[9]*Charles University, Faculty of Maths and Physics, Prague, Czech Republic*
[10]*China Institute of Atomic Energy, Fangshan, Beijing, China*
[11]*Christopher Newport University, Newport News, VA, USA*
[12]*Department of Physics, Columbia University, New York, NY, USA*
[13]

[14]*Czech Technical University in Prague, Faculty of Nuclear Sciences and Physical Engineering, Czech Republic*
[15]*Duquesne University, Pittsburgh, PA, USA*
[16]

[17]*Florida International University, Miami, FL, USA*
[18]*Georgia State University, Atlanta, GA, USA*
[19]*School of Physics and Astronomy, University of Glasgow, Glasgow, UK*
[20]*GSI Helmholtzzentrum fuer Schwerionenforschung, Darmstadt, Germany*
[21]*The George Washington University, Washington, DC, USA*
[22]

[23]

[24]*Racah Institute of Physics, Hebrew University, Jerusalem, Israel*
[25]*Université Paris-Saclay, CNRS/IN2P3, IJCLab, Orsay, France*
[26]*Institute of Modern Physics, Chinese Academy of Sciences, Lanzhou, Gansu, China*
[27]

[28]*Iowa State University*
[29]

[30]

[31]*Jazan University, Gizan, Jazan.*
[32]

[33]

[34]

[35]*Graduate School of Science, Kobe University, Kobe, Japan*
[36]

[37]

[38]*Los Alamos National Laboratory, Los Alamos, NM, USA*
[39]

[40]*Lehigh University, Bethlehem, PA, USA*
[41]*Lawrence Livermore National Laboratory, Livermore, CA, USA*
[42]*Morehead State University, Morehad, KY, USA*
[43]*Massachusetts Institute of Technology, Cambridge, MA, USA*

[44]*Mississippi State University, Mississippi State, MS, USA*
[45]*National Cheng Kung University, Tainan, Taiwan*
[46]*National Central University, Chungli, Taiwan*
[47]*Nihon University, CST, Tokyo, Japan*
[48]*New Mexico State University, Las Cruces, NM, USA*
[49]*National Research Nuclear University MEPhI, Moscow, Russian Federation*
[50]*Nuclear Research Center - Negev, Physics Dept., Beer-Sheva, Israel*
[51]*National Tsing Hua University, Hsinchu, Taiwan*
[52]*National Taiwan University, Taipei, Taiwan*
[53]*Old Dominion University, Department of Physics, Norfolk VA, USA*
[53]*Ohio University, Dept. Of Physics and Astronomy, Athens OH, USA*
[55]*Oak Ridge National Laboratory, PO Box 2008, Oak Ridge, TN, USA*
[56]*Pacific Northwest National Laboratory, Richland, WA, USA*
[57]*Pusan National Univeristy, Busan, Republic of Korea*
[58]*Rice University, Houston, TX, USA*
[59]*RIKEN Nishina Center, Wako, Saitama, Japan*
[60]*The State University of New Jersey, Department of Physics and Astronomy, Piscataway, NJ, USA*
61
[62]*Center for Frontiers in Nuclear Science, Department of Physics and Astronomy, Stony Brook University, Stony Brook, NY, USA*
[63]*Department of Physics and Astronomy, Stony Brook University, Stony Brook, NY, USA*
[64]*RIKEN BNL Research Center, Brookhaven National Laboratory, Upton, NY, USA*
65
[66]*Seoul National University, Seoul, Republic of Korea*
[67]*Sejong University, Seoul, Republic of Korea*
[68]*Shinshu University, Matsumoto, Nagano, Japan*
[69]*Sungkyunkwan University, Suwon, Republic of Korea*
70
71
[72]*Tsinghua University, Beijing, China*
[73]*Tsukuba University of Technology, Tsukuba, Ibaraki, Japan.*
[74]*University of Colorado Boulder, Boulder, CO, USA*
75
[76]*University of Connecticut, Storrs, CT, USA*
[77]*University of Houston, Houston, TX, USA*
[78]*University of Illinois, Urbana, IL, USA*
79
80
[81]*Faculty of Mathematics and Physics, University of Ljubljana, Ljubljana, Slovenia*
82
[83]*University of New Hampshire, Durham, NH, USA*
[84]*Department of Physics, University of Oslo, Norway*
[85]*University of Regina, Regina, SK, Canada*
[66]*Seoul National University, Seoul, Republic of Korea*
87
88

[89]*University of Tsukuba, Tsukuba, Japan*
[90]*University of Tennessee, Knoxville, TN, USA*
[91]
[92]*University of Virginia, Charlottesville, VA, USA*
[93]*Department of Physics and Astronomy, Vanderbilt University, Nashville, TN, USA*
[94]
[95]*Virginia Union University, Richmond, VA, USA*
[96]*Wayne State University, Detroit, MI, USA*
[97]*Department of Particle Physics and Astrophysics, Weizmann Institute of Science, Rehovot, Israel*
[98]*William and Mary, Williamsburg, VA, USA*
[99]*Faculty of Science, Yamagata University, Yamagata, Japan*
[100]
[101]*Yonsei University, Seoul, Republic of Korea*
[102]*University of York, York, UK*
[103]*Department of Physics, Faculty of Science, University of Zagreb, Zagreb, Croatia*